SINGLE- AND MULTIPLE-SCATTERING MECHANISMS IN HIGH-ENERGY NUCLEAR COLLISIONS

Thesis by

Robert Lee Hatch

In Partial Fulfillment of the Requirements

for the Degree of

Doctor of Philosophy

California Institute of Technology

Pasadena, California

1980

(Submitted August 22, 1979)

ACKNOWLEDGMENTS

This thesis would not have been possible without the ideas and keen insight of my advisor, Professor Steven E. Koonin, and most of this work was carried out in close collaboration with him. He is an excellent teacher and warm individual, and I appreciate his availability when I needed help and his generosity in providing me with opportunities to attend conferences and workshops.

I would like to thank the professors, staff, and students of Caltech and especially of Kellogg Radiation Lab for providing a stimulating and pleasant atmosphere in which to live and work. Caltech has helped me in the form of teaching and research assistantships and tuition scholarships. This work was supported in part by the National Science Foundation [PHY76-83685].

In the preparation of this work we benefitted by close contact with Drs. Nagamiya and Tanihata and their collaborators (Nagamiya 1977, Tanihata 1979) at Lawrence Berkeley Lab. We appreciate their sharing with us much of their data prior to publication. I also acknowledge gratefully the prompt and efficient efforts of Vere Snell (Ext. 1801) and Ruth Stratton (Ext. 1826) for the typing of the manuscript and Heather Marr (794-9008) for the illustration.

It is to my family that this thesis is dedicated. I have benefitted immeasurably throughout my life from the love, teachings, and encouragement of my parents, Helen and Terrance Hatch. My father has been a special example to me of integrity and hard work.

My son, Richard, has provided me with many moments of joy during the past year. And finally a very special appreciation goes to my lovely wife, Kristine, for her love, support, and understanding and for making our stay here a truly beautiful experience.

ABSTRACT

We study the production of energetic protons from relativistic nuclear collisions using two approaches, the hard-scattering model and an intranuclear cascade model. The hard-scattering model combines the simplified kinematics of single scatterings and the effects of the momentum distribution for nucleons in the nucleus to provide a parameter-free description of a nucleus-nucleus collision. We use free nucleon-nucleon cross sections to describe the individual NN interactions. Good agreement with experiment is obtained in this model for the high-momentum regions of the inclusive proton spectra from collisions at 800 MeV/nucleon. Crucial to this success is the inclusion of a high-momentum tail in the momentum distribution. This model is also applied to explain the observed two-proton azimuthal correlations from these systems and, with simple assumptions, to estimate the single-scattering component of the inclusive proton spectra. This latter is at least 37% in the lower momentum regions of the spectra analyzed. We also present calculations of the one- and two-particle inclusive spectra using forms for the momentum distribution obtained both from the analysis of proton-nucleus backscattering data and from theory. Finally, we use a simple cascade model to calculate the inclusive proton spectra at 180^{o} from 600 MeV proton-nucleus collisions. The nucleus is assumed to be a Fermi gas of uniform density, and we neglect the excitation of resonances in the

intermediate state and the reflection and refraction of cascade nucleons due to variations in the mean nuclear potential. The calculated results are below the experimental values and imply the presence of other reaction mechanisms.

TABLE OF CONTENTS

Acknowledgments ii

Abstract iv

Table of Contents vi

1. INTRODUCTION 1

1.1 Nucleus-Nucleus Collisions, Experiment 1

1.2 Theoretical Methods for Nucleus-Nucleus Collisions 2

1.3 Proton-Nucleus Collisions 7

2. GENERAL THEORY OF THE MODEL 9

2.1 The Bethe-Salpeter Equation 9

2.2 Derivation of the Basic Hard-Scattering Formula 11

2.3 The Electromagnetic Form Factor 13

2.4 Modification Due to the Scattering of Multiple Pairs of Nucleons 14

2.5 Effects of Final-State Interactions 18

3. CALCULATION OF THE SINGLE-PARTICLE INCLUSIVE PROTON AND PION SPECTRA 20

3.1 General Procedure 20

3.2 Description of the Calculation 20

3.3 Inclusion of Pion Production 21

3.4 Normalization 22

3.5 Description of Results and Comparison with Experiment 24

3.6 Summary 29

4. TWO-PROTON CORRELATIONS 31

4.1 Expected Results 31

4.2 Experimental Results 31

4.3 Correlations from the Hard-Scattering Model 33

5. PROTON-NUCLEUS BACKSCATTERING IN A MULTIPLE-COLLISION MODEL 39

5.1 The Theoretical Models 39

5.2 Simple Considerations 40

5.3 Derivation of the Basic Equations 42

5.4 Description of the Calculation 47

5.5 Comparison of the Results with Experiment 55

6. SUMMARY AND CONCLUSION 58

Appendix A Monte Carlo Methods 63

A.1 Integration 63

A.2 Direct Simulation 65

Appendix B Nucleon-Nucleon Cross Sections 67

B.1 Angular Distributions for Proton-Proton Collisions 67

B.2 Angular Distributions for Proton-Neutron Collisions 68

B.3 Total Interaction Cross Sections for Proton-Proton Collisions 69

B.4 Total Interaction Cross Sections for Neutron-Proton Collisions 70

B.5 Total Elastic Cross Sections for Nucleon-Nucleon Collisions 70

Appendix C Kinematics of the Cascade Calculation 72

References 77

Tables 80

Figures 81

1. INTRODUCTION

In recent years there has been considerable experimental and theoretical activity in the field of high-energy (0.2 - 2.0 GeV/nucleon) nuclear collisions. A wealth of data has been accumulated at these energies for projectiles varying in size from p to Ar (Saudinos 1974, Papp 1975, Frankel 1976, Westfall 1976, Brody 1977, Gosset 1977, Nagamiya 1977). In this chapter we shall describe some of the prominent features of the inclusive proton and pion spectra and also many of the theoretical models proposed to explain them. Then we will point out the need for the present study and its relation to earlier work.

1.1 Nucleus-Nucleus Collisions, Experiment

There are several reasons for the high interest in relativistic heavy-ion collisions. Because of the energetic reactions between large numbers of nucleons, it is possible that substantial build-ups of density and temperature occur in the nuclear matter, and under the assumption of many randomizing collisions between participating nucleons, that local equilibrium is reached during a collision. Thus, a major reason for the excitement in the field is the hope that these collisions will tell us about the nuclear equation-of-state $E(\rho,T)$, the energy per nucleon as a function of density and pressure, for values far from the normal nuclear density ρ_o. At present, the experimental knowledge of E is limited to the region at ρ_o for $T = 0$. Another point of interest, which will become clear in this paper, is that high-energy nuclear collisions may yield information about the momentum distribution of nucleons in the ground state nucleus, and something that is related to this, the correlations

between nucleons.

In discussing a collision involving two heavy ions, it is convenient to divide up the momentum space of the fragments into three distinct regions. The fragmentation regions near the momenta of the target and projectile which are dominantly populated by their breakup after the collision, and the central region intermediate between the target and projectile momenta and at large transverse momentum. It is this central region, populated by violent processes in the collision, which we consider here.

As an example of some of the fine data available (taken by Nagamiya et al. (1977)) we refer the reader ahead to Figs. 1, 10 and 11, which show the inclusive proton and pion spectra for various targets and projectiles at 800 MeV/nucleon. Particularly instructive is the global plot for Ne + Pb in Fig. 1, where contours of constant invariant cross section are plotted in rapidity space.* Among the salient features of these data are the large numbers of protons at very high P_T, far past the kinematically allowed region for a free nucleon-nucleon scattering, the tendency toward symmetry about half the beam rapidity at large P_T, and, though not evident here, the independence of the decay of the cross sections at large P_T on the size of the target and projectile (Nagamiya 1977). These points will be discussed further in relation to the various theoretical models.

1.2 Theoretical Methods for Nucleus-Nucleus Collisions

A great variety of models have been proposed to explain the spectra from relativistic heavy-ion collisions. Many of these differ greatly in

*For a definition and discussion of rapidity, see Section 3.5.

their underlying assumptions. At one extreme are the equilibrium models (Westfall 1976, Gosset 1977, Myers 1977, Amsden 1977, 1977a) which assume that local equilibrium is attained due to the many collisions between large numbers of nucleons. At the other extreme are the hard-scattering or single-collision models (Koonin 1977 and Schmidt 1977) which assume that a major contribution to the spectra results from nucleons which are emitted after undergoing only one collision. Between these two extremes are the multiple-collision or cascade models (Bondorf 1976, Amsden 1977, Hüfner 1977, Smith 1977, Randrup 1978).

Of the equilibrium models, the first and probably the simplest model proposed is the fireball model (Westfall 1976 and Gosset 1977). It combines geometry and thermodynamics in a simple, parameter-free way. At each impact parameter, the nuclei make straight-line, cylindrical cuts through each other, thus dividing the nucleons into two groups: the "participants" in the interaction region between the cuts, and the "spectators" in the residual nuclei. All of the available kinetic energy of the participants in their c.m. system is assumed to be turned into heat, and this "fireball" then decays according to a Boltzmann momentum distribution. With the further assumption of chemical equilibrium, this can be extended to include the production of pions and composites. The fireball and related firestreak (Meyers 1977) models have enjoyed remarkable success in describing the inclusive spectra of protons, pions, and composites for a variety of energies and system sizes.

Other equilibrium models (Amsden 1977, 1977a) solve the continuity equations for the nucleon number, momentum, and energy densities of relativistic hydrodynamics. Input of the equation-of-state $E(\rho,T)$ allows the direct study of its effects. These models have also had a degree of success explaining the inclusive proton spectra.

The underlying assumptions of the equilibrium models exclude any effects due to the individual two-body reactions. In a discussion of experimental two-proton correlations in Chapter 4, it will be shown that a serious limitation of these models in their present form is their inability to describe a large contribution to the spectra due to single scatterings.

Under the assumption that nucleus-nucleus collisions can be described microscopically by a succession of independent single-particle collisions, the multiple-collision models present an attractive approach (Bondorf 1976, Amsden 1977, Hüfner 1977, Smith 1977, Randrup 1978). Although the cascade models are generally more complex than the equilibrium models, they can be used to study the assumptions of thermalization by taking "snapshots" of the momentum distribution of the interacting nucleons at different times during a simulated collision. Also included is the single-scattering component of the spectra. While there are far too many approaches to discuss here in detail, the more successful cascade models include the following ingredients: simulation of the cascade by Monte Carlo techniques, production of pions through the $\Delta(1232)$ resonance, choice of the scattering angle of individual NN scatterings by the experimental NN cross sections, and the use of a sharp Fermi momentum distribution for nucleons in the nucleus. These models have been successful in

reproducing much of the inclusive proton and pion spectra. However, besides possible disadvantages due to complexity or cost of implementation, these models do not include effects due to the high momentum components in the momentum distribution for nucleons in the nucleus (see Zabolitzky 1978).

The equilibrium and cascade models are able to produce protons with large transverse momentum through the many individual collisions that occur among the nucleons. Each successive collision is able to populate larger regions of momentum space. However, the independence of the decay of the spectra at large P_T on the target and projectile, and the symmetry of the spectrum about half the beam rapidity at large P_T (as seen in Fig. 1) suggest that a simpler mechanism, one independent of the number of nucleons in the nuclei, may be important here. These features can be explained easily if the dominant mechanism contributing to this region is the single, hard collision of two nucleons. This question, which is addressed in the present work, is of fundamental importance in our understanding of these processes. Indeed, if the hard scattering mechanism is dominant at large P_T, then it is useless to attempt to study the properties of equilibrium here.

In order for the hard-scattering mechanism to populate regions at large P_T, it is necessary to include high-momentum components in the momentum distribution for nucleons in the nucleus. Experimentally, the form of this distribution is not known. Quasi-elastic electron scattering is not sensitive to this high-momentum tail (Moniz 1971). However, when interpreted in terms of a single scattering model (Amado

1976), recent back-angle proton-nucleus data provide a sensitive test of the high-momentum behavior of the distribution and are consistent with an exponential falloff up to 1.3 GeV/c (Brody 1977, Frankel 1977). We use a form for the distribution (Eq. 3-6) which is consistent with the proton-nucleus data (Amado 1976) and which has been motivated by an exact, though unphysical calculation involving a one-dimensional system of bosons interacting via a delta potential. At the time we undertook our study this was the only available form, but since then theoretical calculations for the momentum distribution have been made using many-body theory for finite nuclei with realistic nuclear potentials (Zabolitzky 1978). These also have an approximate exponential falloff with about the same slope (see Section 3.5 and Fig. 12 for more details). For comparison, we use both forms in the calculations presented here.

There have been earlier efforts to calculate the proton and pion spectra with the single-scattering mechanism. The calculation of Koonin (1977) uses a sharp Fermi momentum distribution, and, though able to describe many features of the inclusive proton spectra, eventually it fails for regions at large P_T. Pion production is not included, and the kinematics governing energy and momentum conservation differs from the present treatment. Calculations of two-nucleon correlations due to the two-body kinematics are also first presented here. The approach of Schmidt and Blankenbecler (1977) differs from ours essentially in the evaluation of Eq. (2-7). Their field theoretical analysis of the momentum distribution is applicable only in the extreme asymptotic region far from the data considered here. Equation (2-7) is also approximated in the

asymptotic limit. Finally, very simple parametrizations are used to describe the N+N → N+X and N+N → π+X processes.

1.3 Proton-Nucleus Collisions

Proton-nucleus collisions provide an important testing ground for our ideas on nucleus-nucleus collisions. If a model can be extended successfully from the regime of proton-nucleus to nucleus-nucleus collisions without additional assumptions or parameters, then this places much more validity on the results. Both the cascade and hard-scattering models appear to meet this requirement for the regions tested thus far. Multiple-collision models in the Glauber approximation (Glauber 1959, Saudinos 1974) for small angle scattering and in the full Monte Carlo cascade treatment (Chen 1968) have long been used successfully for proton-nucleus collisions. Hard-collision models with an exponential tail in the momentum distribution have more recently proven to be a viable approach (Amado 1976, Brody 1977, Frankel 1977).

There is one regime in proton-nucleus collisions which provides a severe test for any model. In recent years data have been taken on the production of large-momentum protons at backward angles (Frankel 1976, Brody 1977 ; see Fig. 16), far into the kinematically forbidden region for the scattering of a proton on a free nucleon with momentum up to the Fermi momentum, $P_F \sim 270$ MeV/c. Among the mechanisms proposed to produce these energetic protons are the coherent scattering from clusters (Fujita 1977), multiple NN collisions, and, as pointed out earlier, the hard-collision model (Amado 1976, Brody 1977, Frankel 1977). The cluster and hard-collision models give quantitative agreement with

experiment. The results for the multiple-collision model are not as yet known, due to the difficulty of producing these rare events in a Monte Carlo calculation, although estimates have been made (Kopeliovich 1977). The solution of this problem will occupy the final part of this thesis.

The outline for this thesis proceeds as follows. In Chapter 2 we explain the theory behind the hard-scattering model and derive the basic equations. A description of the calculation of the inclusive proton and pion spectra for nucleus-nucleus collisions and the comparison of these with experiment is made in Chapter 3. The experimental results for two-proton correlations and the predictions of the hard-scattering model are presented in Chapter 4. We depart from the hard-scattering model in Chapter 5 to calculate the back-angle proton spectra from proton-nucleus collisions in a multiple-collision model. Finally, we summarize the results and present our conclusions in Chapter 6.

2. GENERAL THEORY OF THE MODEL

2.1 The Bethe-Salpeter Equation

A relativistic bound-state system may be conveniently described by the Bethe-Salpeter wave function (Salpeter 1951). We give here a heuristic derivation of the Bethe-Salpeter equation for a two-particle bound state, and in so doing the rules for its implementation will be apparent. A rigorous derivation may be found in Gell-Mann (1951). The derivation will be for quantum-electrodynamics (QED), although the generalization to other systems is straightforward. We adopt the notation and rules for evaluating Feynman diagrams from Bjorken (1964). With these rules one can easily write down the matrix element of an arbitrary diagram such as Fig. 2. We define the wave functions $\bar{\Psi}^{(C)}$ and $\Psi^{(B)}$ to be the contribution of the graph up to the dotted lines (including the particle propagators). These wave functions then have 16 spinor components (for QED) and can be used to write the matrix element of the graph as

$$M = \int \frac{d^4p_3}{(2\pi)^4} \int \frac{d^4p_5}{(2\pi)^4} \bar{\Psi}^{(C)}(p_5, P-p_5) \left\{ \frac{i\gamma_\mu e^2 \gamma^\mu}{(p_3-p_5)^2+i\varepsilon} \right\} \Psi^{(B)}(p_3, P-p_3), \quad (2\text{-}1)$$

where the above integrals are over each momentum not fixed by momentum conservation. It is also clear that $\Psi^{(B)}$ can be written in terms of $\Psi^{(A)}$ in Fig. 2 as

$$\Psi^{(B)}(p_3, P-p_3) = iS_F(p_3) iS_F(P-p_3) \int \frac{d^4p_1}{(2\pi)^4} \left\{ \frac{i\gamma_\mu e^2 \gamma^\mu}{(p_1-p_3)^2+i\varepsilon} \right\} \times \Psi^{(A)}(p_1, P-p_1) \quad , \quad (2\text{-}2)$$

where $iS_F(p) = \frac{i(\not{p}+m)}{p^2 - m^2 + i\varepsilon}$ is the internal Fermion propagator. Now we define an irreducible graph as one which cannot be split into two simpler graphs by drawing a line which cuts no photon line and both of the particle lines once. Thus, a diagram of any complexity can be constructed from sequences of irreducible graphs. We show several of the lowest order irreducible graphs in Fig. 3. (Diagrams (d) and (e) are considered irreducible, since they must be included with diagram (c) in renormalization (Bjorken 1964a).) Let $G^{(n)}$ denote the contribution of the n^{th} diagram without the external propagators (i.e., $G^{(a)}(p_3,p_1) = \frac{i\gamma_\mu e^2 \gamma^\mu}{(p_1-p_3)^2+i\varepsilon}$). Also, let $\Psi^{(m_1,m_2,\cdots,m_i)}(p_1,P-p_1)$ denote the wave function which has diagrams $(m_1,m_2,\cdots,m_i)$ as its only contribution. Then

$$\Psi^{(n,m_1,m_2,\cdots,m_i)}(p_3,P-p_3) = iS_F(p_3)\, iS_F(P-p_3)$$

$$\times \int \frac{d^4p_1}{(2\pi)^4} G^n(p_3,p_1)\, \Psi^{(m_1,m_2,\cdots,m_i)}(p_1,P-p_1) \quad . \tag{2-3}$$

The bound state wave function $\Psi(p_1,P-p_1)$ can be considered to be made up of an infinite sequence of all possible combinations of irreducible diagrams, since it is bound for an infinitely long time and can have any combination of exchanged quanta. We then formally sum Eq. (2-3) over all $n,m_1,m_2,\cdots,m_i$ and let $i \to \infty$ to obtain the integral equation

$$\Psi(p_3,P-p_3) = iS_F(p_3)\, iS_F(P-p_3) \int \frac{d^4p_1}{(2\pi)^4} G(p_3,p_1)\, \Psi(p_1,P-p_1), \tag{2-4}$$

where $G(p_3,p_1) = \sum_{n=1}^{\infty} G^{(n)}(p_3,p_1)$. This is the Bethe-Salpeter equation

in momentum space. It is also convenient to define the vertex function Φ by

$$\Psi(p_3, P - p_3) = iS_F(p_3) iS_F(P - p_3)\, \Phi(p_3, P - p_3) \quad . \tag{2-5}$$

If the coupling constants are small, such as in QED, then one can cut off the sum in Eq. (2-4) at lower orders. The physical idea is that, for a weak coupling constant, the probability to have a single exchanged quantum at a given time is small but very much smaller still to have two virtual quanta in the field at the same time. The use of $G^{(1)}$ alone is called the ladder approximation.

2.2 Derivation of the Basic Hard-Scattering Formula

We now derive an expression for the inclusive nucleon cross section for a nucleus-nucleus collision, using the knockout diagram of Fig. 4. For simplicity we neglect all spin effects as well as the isotopic distinction of the nucleons. The colliding nuclei are designated by four-momenta P and P', the interacting nucleons by p and p', and the residual nuclei will be considered to be in a definite state and have four momenta P-p and P'-p'. Using the Bethe-Salpeter vertex functions one can write the matrix element for this process as

$$M(P, P' \to P-p, P'-p', k, k') = m(p, p' \to k, k')$$

$$\times\ iS(p')\, \Phi'(p', P'-p)\, iS(p)\, \Phi(p, P-p) \quad , \tag{2-6}$$

where $iS(p) = \dfrac{i}{p^2 - m^2}$ is the internal propagator for spinless "nucleons" and $m(p, p' \to k, k')$ is the matrix element for the nucleon-nucleon interaction. Notice that only one propagator accompanies each vertex function,

since the residual nucleus is on shell. The inclusive cross section is (Schmidt 1977)

$$E(k)\frac{d\sigma}{d^3k} = \frac{1}{2E(P)\,2E(P')\left|\vec{V}-\vec{V}'\right|}\int |M|^2\,\pi\delta^4(p+p'-k-k')$$

$$\times\ \frac{d^3(P-p)}{2(2\pi)^3\,E(P-p)}\,\frac{d^3(P'-p')}{2(2\pi)^3\,E(P'-p')}\,\frac{d^3k'}{2(2\pi)^3\,E(k')} \qquad (2\text{-}7)$$

$$= \int d^3p\,d^3p'\,f(\vec{p})\,f'(\vec{p}')\,P\,E(k)\frac{d\sigma}{d^3k}(p+p'\to k+k')\ ,$$

where $$f(\vec{p}) \equiv \frac{|\Phi(p,P-p)|^2(p\cdot P)}{2(2\pi)^3\,E(P-p)\,P^2(p^2-m^2)^2}\quad (p_o = E(P)-E(P-p))\ ,$$

$$P \equiv \frac{P^2P'^2}{(p\cdot P)(p'\cdot P')}\,\frac{\lambda((p+p')^2,p^2,p'^2)}{\lambda((P+P')^2,P^2,P'^2)}\ ,$$

$$\lambda(x,y,z) \equiv (x^2+y^2+z^2-2xy-2xz-2yz)^{1/2}\ ,$$

and

$$E(k)\frac{d\sigma}{d^3k}(p+p'\to k+k') \equiv \int \frac{|m(p+p'\to k+k')|^2\,\pi\delta^4(p+p'-k-k')}{2\lambda((p+p')^2,p^2,p'^2)}$$

$$\times\ \frac{d^3k'}{2(2\pi)^3\,E(k')}\ .$$

Here, $\lambda((p+p')^2,p^2,p'^2)$ is an off shell generalization of the flux factor; its value is $2E(p)\,E(p')\left|\vec{v}-\vec{v}'\right|$ for on-shell, colinear particles. This equation has a simple probabilistic meaning if one associates $f(\vec{p})$ with the probability distribution for finding a nucleon of momentum $\vec{p}$

in the nucleus. $E(k)\frac{d\sigma}{d^3k}(p+p' \to k+k')$ is related to the probability for the two nucleons to scatter into the final states k and k', and P is related to the fluxes of the colliding particles.

The knockout diagram of Fig. 5 for proton-nucleus scattering is also evaluated easily and is given by Eq. (2-7) with $f'(\vec{p}') = \delta^3(\vec{P}' - \vec{p}')$, as expected.

2.3 The Electromagnetic Form Factor (Sivers 1976)

We will now show that the definition of $f(\vec{p})$ in Eq. (2-7) is consistent with its interpretation as the probability for finding a particle with momentum p in the nucleus. This is done by demonstrating that the electromagnetic form factor at zero momentum transfer is

$$A = F(q^2=0) = \int d^3\vec{p}\, f(\vec{p}) \quad , \tag{2-8}$$

where A is the number of nucleons in the nucleus. We evaluate the form factor in the impulse approximation of Fig. 6, where we are restricting ourselves to the Breit frame defined therein. The form factor is written as

$$(P+P+q)^\mu F(q^2) = -i \int \frac{d^4(P-k)}{(2\pi)^4} \frac{(k+k+q)^\mu\, \Phi^+(k+q,P-k)\, \Phi(k,P-k)}{[(k+q)^2-m^2+i\varepsilon][(P-k)^2-M^2+i\varepsilon][k^2-m^2+i\varepsilon]} \quad , \tag{2-9}$$

where m is the nucleon mass and M is the mass of the residual nucleus. It is now clear why F(0) = A --at zero momentum transfer the structure of the nucleus is not probed, but behaves as a single particle of "charge" A. Since M >> m, we expect that the dominant contribution to the integral occurs for $(P-k)^2 = M^2$. The $P_o - k_o$ integration is performed by

completing the contour in the lower half complex plane and picking up the dominant pole at $P_o - k_o = \sqrt{(\vec{P}-\vec{k})^2 + M^2} - i\varepsilon$. Since the ingoing and outgoing mass is identical, we have the relation $P^2 = P'^2 = (P+q)^2$ or $P\cdot q = q^2/2$. Contracting each side of Eq. (2-9) with P_μ yields

$$F(q^2) = \int \frac{d^3k}{2(2\pi)^3 E(P-k)} \frac{2P\cdot k + (q^2/2)}{2P^2 + (q^2/2)} \frac{\Phi^+(k+q,P-k)\,\Phi(k,P-k)}{[(k+q)^2 - m^2][k^2 - m^2]} \quad . \quad (2\text{-}10)$$

Now in the Breit frame, $q^2 = 0$ implies that $q = (0,\vec{q}) = (0,0)$. Therefore,

$$F(0) = \int \frac{d^3k}{2(2\pi)^3 E(P-k)} \frac{P\cdot k}{P^2} \frac{|\Phi(k,P-k)|^2}{[k^2-m^2]^2}$$

$$= \int d^3k\, f(\vec{k}) \qquad (k_o = E(P) - E(P-k)) \quad . \quad (2\text{-}11)$$

Since this is a relativistically invariant form, it holds true in any frame.

2.4 Modification Due to the Scattering of Multiple Pairs of Nucleons

Because of the spatial density of the colliding nuclei, it is clear that even in the knockout picture (neglecting final-state interactions), the process shown in Fig. 4 will not give the only major contribution, but must be modified to allow multiple pairs of nucleons to scatter in each nucleus-nucleus collision. We now show how this modification is made by evaluating the diagram in Fig. 7, which represents two pairs of nucleons scattering with no final state interactions.

Using the rules described above, the matrix element for this process can be written as

$$M(A,B \to \alpha,\beta,k_1,k_2,k_3,k_4) = \int \frac{d^4b_2}{(2\pi)^4}\ G(b_2) \quad , \tag{2-12}$$

where

$$G(b_2) = \frac{\Phi_A(a_1,a_2,\ A-a_1-a_2)}{(a_1^2 - m^2)(a_2^2 - m^2)}\ m(a_2,b_2 \to k_3,k_4)\ m(a_1,b_1 \to k_1,k_2)$$

$$\times\ \frac{\Phi_B(b_1,b_2,\ B-b_1-b_2)}{(b_1^2 - m^2)(b_2^2 - m^2)} \quad ,$$

$$a_1 = k_1+k_2 + b_2+\beta-B \quad ,$$

$$a_2 = k_3+k_4-b_2 \quad ,$$

and

$$b_1 = B-\beta-b_2 \quad .$$

The invariant differential cross section is then

$$E(k_1)\ \frac{d\sigma}{d^3k_1} = \frac{1}{2E(A)2E(B)\left|V_A-V_B\right|} \int \frac{d^3\alpha}{2(2\pi)^3E(\alpha)}\ \frac{d^3\beta}{2(2\pi)^3E(\beta)}\ \frac{d^3k_2}{2(2\pi)^3E(k_2)}$$

$$\times\ \frac{d^3k_3}{2(2\pi)^3E(k_3)}\ \frac{d^3k_4}{2(2\pi)^3E(k_4)} \left[\int \frac{d^4b_2'}{(2\pi)^4}\ G^*(b_2')\right]\left[\int \frac{d^4b_2}{(2\pi)^4}\ G(b_2)\right]$$

$$\times\ \pi\delta^4(A+B-\alpha-\beta-k_1-k_2-k_3-k_4). \tag{2.13}$$

We now assume that the vertex function can be written in the separable form

$$\Phi(a_1,a_2,\ A-a_1-a_2) = \Phi(a_1,\ A-a_1)\ \Phi(a_2,\ A-a_2) \quad . \tag{2-14}$$

This is a reasonable assumption for large nuclei, where a given nucleon

is on the average affected little by any other nucleon. Then $G(b_2)$ can be written as

$$G(b_2) = g(B-\beta-b_2,k_1,k_2)\; g(b_2,k_3,k_4) \quad , \tag{2-15}$$

where

$$g(x,k,k') \equiv \frac{\Phi_A(k+k'-x,\; A+x-k-k')}{[(k+k'-x)^2 - m^2]}\; m(k+k'-x,\; x\to k,k')$$

$$\times \frac{\Phi_B(x,B-x)}{[x^2 - m^2]} \quad .$$

By defining the variables

$$a_2' = k_3+k_4-b_2' \quad ,$$

$$p = B-\beta-b_2 \quad ,$$

and

$$p' = A-\alpha-a_2' \quad ,$$

a change of variables allows Eq. (2-13) to be written as

$$E(k_1)\frac{d\sigma}{d^3k_1} = \frac{1}{2E(A)2E(B)|V_A-V_B|}\int \frac{d^3p}{2(2\pi)^3}\frac{d^3p'}{2(2\pi)^3}\frac{d^3k_2}{2(2\pi)^3E(k_2)}$$

$$\times \frac{d^3k_3}{2(2\pi)^3E(k_3)}\frac{d^3k_4}{2(2\pi)^3E(k_4)}\frac{d^4a'_2}{(2\pi)^4}\frac{d^4b_2}{(2\pi)^4}\; g^*(k_1+k_2-p',k_1,k_2)$$

$$\times\; g^*(k_3+k_4-a_2',k_3,k_4)$$

$$\times \frac{g(p,k_1,k_2)g(b_2,k_3,k_4)\;\pi\delta(a_2'+p'+p+b_2-k_1-k_2-k_3-k_4)}{E(A-p'-a_2')\;E(B-p-b_2)} \quad . \tag{2-16}$$

We next assume that the functions $g(x,k_3,k_4)$ are sharply peaked in x so

that we may take the slowly varying functions of x out of the integral. This assumption is made plausible by the relation of the vertex functions to a momentum distribution. We replace $\alpha_o = E(A-p'-a_2')$ by $E(A-p')$ since we can neglect any reasonable value of $\vec{a}_2'$ compared to M_α for moderately sized nuclei. Also, p' depends on a_2' only through $p_o' = A_o-\alpha_o-a_{2o}'$. We thus take $g^*(k_1+k_2-p',k_1,k_2)$ out of the integral a_2' with a_{2o}' replaced by an average $\bar{a}_o$. The same arguments also hold for $\beta_o = E(B-p-b_2)$ and $g(p,k_1,k_2)$. By observing that the peak in the b_2 and a_2' integrals occurs at $b_2' = k_3+k_4-a_2'$ for each k_3 and k_4, we replace the delta function by $\delta^4(p'+p-k_1-k_2)$. Our final result may be written as

$$E(k_1)\frac{d\sigma}{d^3k_1} \simeq \frac{N}{2E(A)\ 2E(B)\left|\vec{V}_A-\vec{V}_B\right|} \int \frac{d^3p}{2(2\pi)^3E(B-p)} \frac{d^3p'}{2(2\pi)^3E(A-p')}$$

$$\times \frac{d^3k_2}{2(2\pi)^3E(k_2)} \frac{\left|\Phi_A(p',A-p')\right|^2}{[p'^2-m^2]^2} \frac{\left|\Phi_B(p,B-p)\right|^2}{[p^2-m^2]^2} \left|m(p,p' \to k_1,k_2)\right|^2$$

$$\times \pi\delta^4(p+p'-k_1-k_2) \quad , \qquad (2\text{-}17)$$

where

$$N = \int \frac{d^3k_3}{2(2\pi)^3E(k_3)} \frac{d^3k_4}{2(2\pi)^3E(k_4)} \left| \int \frac{d^4b}{(2\pi)^4} \frac{\Phi_A(k_3+k_4-b,\ A-k_3-k_4+b)}{[(k_3+k_4-b)^2-m^2]} \right.$$

$$\left. \times\ m(k_3+k_4-b,b \to k_3,k_4) \frac{\Phi_B(b\ ,B-b\ )}{[b^2-m^2]} \right|^2 \quad ,$$

$$p_o' = E(A) - E(A-p') - \bar{a}_o \quad ,$$

and $$p_o = E(B) - E(B-p\ ) - \bar{b}_o \quad .$$

We see that this differs from Eq. (2-7) only in the overall normalization

and the energy available to scatter in p_o and p_o'. One expects this intuitively, since the scattering of an extra pair of nucleons should affect the energy available to the other two as well as the total probability to occur, although this average energy shift is not expected to be great when the nuclei are large and each nucleon affects any other nucleon very little. However, because the average multiplicity of scattered nucleons in most nucleus-nucleus collisions is greater than two (an experimental estimate is 7 for C+C and 19 for Ar+KCl (Tanihata 1979)), a modification of the normalization of the basic knockout equation (Eq. 2-7) due to the contribution of the scattering of multiple pairs of nucleons (as in Fig. 7) appears necessary in a correct treatment. In Section 3.4 in the next chapter, we discuss our approach to the normalization.

2.5 Effects of Final-State Interactions

It might be expected that at large bombarding energies the effect of final-state interactions on the knockout process is small. However, it has been shown that this may not be the case but that final-state interactions might have to be included on an equal footing (Amado 1977). Using general arguments of the orthogonality of the discrete and continuum states of the target nucleus, what was actually shown is this: If in the knockout picture a probe imparts a momentum transfer q to a constituent particle in the target with momentum p (resulting in a final momentum k=p+q), then the leading term for large k is exactly canceled by the contribution from final-state interactions.

The diagram in Fig. 8 includes the effects of final-state interactions. Because of the complexity of the matrix element M_2, the exact

inclusion of this contribution in the cross section is not possible at this time. However, we can include possible effects of final-state interactions in our treatment by replacing $f(\vec{p})$ in Eq. (2-7) with a modified or "effective" momentum distribution $f_e(\vec{p})$. That most of the effects can be included in this way is justified to some degree by the following arguments: The inclusive cross section calculated from Eq. (2-7) is not affected a great deal by variations in $\frac{d\sigma}{d\Omega}$ (N+N → N+N) (even an isotropic distribution does not change the results substantially for most regions of the spectrum, the region at 90° in the center-of-mass being affected most), but depends most strongly on the kinematical constraints (available energy, etc.) and the form for the distribution $f(\vec{p})$. The kinematics of the final states are the same for both pictures (as seen in Figs. 4 and 8) and in summing over the phase space for unobserved particles it is easy to see that the result can be written in the form of Eq. (2-7), but without the factorization of the matrix element for NN scattering. Assuming that the interaction M_2 does not have a strong focusing effect into a particular direction away from the results of M_1, then Eq. (2-7) gives a good approximation to the single particle inclusive cross section with an effective momentum distribution $f_e(p)$ replacing $f(p)$. This argument does not, of course, hold for two-particle coincidence measurements, since the simple two-body kinematics is lost in the final-state interactions.

3. CALCULATION OF THE SINGLE-PARTICLE INCLUSIVE PROTON AND PION SPECTRA

3.1 General Procedure

In this section we describe a calculation using the hard-scattering mechanism of Fig. 4. We evaluate Eq. (2-7) using the Monte-Carlo methods described in Appendix A. Because of the simple probabilistic meaning of Eq. (2-7), it is easy to use Monte Carlo simulation, and the advantages of this approach are several: The entire spectrum is calculated in a single run; pion production can be easily included through simulation of delta production and decay; two particle correlations are also analyzed simply. A possible disadvantage is the increase in statistical errors for events with small cross section (which is also inherent in the experimental situation). These points will become clear when the actual computation is described in detail below. To help guide the reader, the arrangement in the computer code of the following description of the calculation is shown diagrammatically as a flow chart in Fig. 9.

3.2 Description of the Calculation

The momenta of the colliding nucleons are chosen in the center of mass of each of the target and projectile nuclei according to the momentum distribution $f(\vec{p})$. The residual nucleus recoils with momentum $-\vec{p}$, thus specifying the off-shell energy of the interacting nucleons of mass m as

$$p_o = Am - \left\{\left[(A-1)m + \bar{\varepsilon}\right]^2 + \vec{p}^{\,2}\right\}^{1/2} , \qquad (3-1)$$

where $\bar{\varepsilon}$ is an average separation energy determined by the specific state

of the residual nucleus and Am is the initial mass of the nucleus. We approximate the nucleon-nucleon off-shell scattering matrix by the experimental N-N cross sections as follows: The four-momenta p and p' are transformed to their center-of-momentum frame, where the angle of scattering is chosen at random from the experimental angular distribution for elastic scattering $\frac{1}{\sigma_{el}} \frac{d\sigma_{el}}{d \cos \theta_{cm}}$. The input is the total available center-of-mass energy $\sqrt{s} = [(p+p')^2]^{1/2}$. The polynomial fits to $\frac{1}{\sigma_{el}} \frac{d\sigma_{el}}{d \cos \theta_{cm}}$ and σ_{el} are presented in Appendix B. The final nucleons with momenta k and k' contribute a weighting factor $P\sigma_{el}(s)$ (which is related to the probability to scatter) to a bin of angular and momentum width $\Delta\theta$ and Δk, where P is the flux factor of Eq. (2-7). Two cases in which the nucleons do not scatter into final states k and k' are for $s < 4m^2$, and when the final states are not compatible with the exclusion principle. For a nucleus with a momentum distribution f(p) (with normalization f(0) = 1), the probability that a final state p is occupied is just f(p). This is equivalent to placing factors of 1 - f(p) in the integral of Eq. (2-7).

3.3 The Inclusion of Pion Production

To include pion production, we assume that all inelastic events proceed through the formation of the $\Delta(1232)$ resonance. In the spirit of the single-collision model, once the delta is produced it decays without further interactions into the pion and nucleon. The weighting factor for this event is $\sigma_{in}P$ where $\sigma_{in} = \sigma_{tot} - \sigma_{el}$ is the inelastic cross section and σ_{tot} is the average of the proton-proton and proton-neutron

total cross sections calculated from Appendix B. The angular distribution for N+N → N+Δ in the N+N center-of-momentum frame is taken to be that for elastic scattering. The mass width of the Δ resonance is included by assuming the probability distribution for formation at a mass M has a Lorentzian shape

$$P(M) = \frac{\Gamma}{(M-1232)^2 + \Gamma^2} \qquad (3\text{-}2)$$

with half width Γ = 60 MeV (Barish-Schmidt 1973).

One must also take into account in a proper way the effects of polarization on the decay of the Δ. We have investigated this effect by adopting two extreme assumptions for the delta decay: (1) no polarization for an isotropic decay, and (2) maximum polarization with a $1/\sin\theta$ distribution (where θ is measured from the beam axis). The results presented in this paper have used the isotropic decay. The effect of polarization in each case was negligible for the inclusive proton spectrum and small for pion production, although there was a slight forward-backward enhancement with corresponding decrease at large transverse momentum for pions. The results shown in Fig. 10 are essentially unchanged with the inclusion of polarization effects.

3.4 Normalization

As explained in Section 2.4, it is necessary to modify the normalization from that given by Eq. (2-7) because of the spatial compactness of nucleons in the nucleus. We propose an intuitive normalization based on geometry and the single scattering assumption, very similar to the participant-spectator concept of the fireball model (Westfall 1976). The

basic assumption is that at each impact parameter b the number of nucleons which scatter N(b) is twice the smaller number of target or projectile nucleons in the straight line trajectory of the overlap region. Thus the entire overlap region is not swept out in a collision since this would require multiple scatterings. Below we derive an analytical expression for the total cross section for spherical nuclei with a uniform nuclear density.

$$\sigma = \int N(\vec{b})\, d^2\vec{b} \,, \tag{3-3}$$

where

$$N(\vec{b}) = \rho \int d^2\vec{s}_1\, d^2\vec{s}_2\, \delta^2(\vec{s}_1 - \vec{s}_2 - \vec{b})\, 2\, \min(a_1, a_2) \,,$$

$$\left(\frac{a_1}{2}\right)^2 = R_1^2 - s_1^2 \,,$$

$$\left(\frac{a_2}{2}\right)^2 = R_2^2 - s_2^2 \,,$$

and $\vec{s}_1$ and $\vec{s}_2$ are centered at nuclei one and two, respectively, in a plane perpendicular to the beam direction, and the integral extends over the total cross-sectional area of each nucleus. R_1 and R_2 are the nuclear radii, and ρ is the particle density with

$$A_1 = \int \rho\, a_1\, d^2\vec{s}_1 = \frac{4\pi R_1^3\, \rho}{3} \,.$$

$\min(a_1, a_2)$ denotes the smaller of a_1 and a_2. Note that the fireball cross section is obtained if $a_1 + a_2$ is exchanged for $2\, \min(a_1, a_2)$ above. The integral over impact parameter $\vec{b}$ is carried out first to obtain

$$\sigma = \rho \int d^{2\rightarrow}s_1 \, d^{2\rightarrow}s_2 \; 2 \min(a_1, a_2)$$

$$= \frac{\rho\pi^2}{2} \int_0^{2R_1} da_1 \int_0^{2R_2} da_2 \; a_1 a_2 \min(a_1, a_2)$$

$$= 2\pi[R_1^2 A_2 - \frac{R_2^2}{5} A_2] \; . \qquad \text{for } R_1 > R_2 \qquad (3\text{-}4)$$

The total proton cross section is then

$$\sigma_p = (\frac{Z_1}{A_1} + \frac{Z_2}{A_2})\pi \; [R_1^2 A_2 - \frac{R_2^2}{5} A_2] \quad \text{for } R_1 > R_2 \; , \qquad (3\text{-}5)$$

where Z_1 and Z_2 are the charges of nuclei one and two, respectively. This simple picture should not be taken to be a serious prediction of the single scattering assumption, since it clearly lacks many physical properties such as a diffuse surface, multiple scatterings, contributions from composites, transparency, etc. In other words, one should not accept or reject the single scattering hypothesis by how closely the normalization resembles experiment in each case. However, in the systems we have looked at, the above normalization works pretty well.

3.5 Description of Results and Comparison with Experiment

The choice of the momentum distribution f(p) is a crucial part of the calculation. As was discussed in Section 2.5 it appears that final state interactions destroy the simple dependence of Eq. (2-7) on the ground state momentum distribution. We have investigated this possibility by comparing results of nuclear collisions using an "effective" momentum distribution obtained from experiment with results using the ground state momentum distribution.

We use an effective momentum distribution

$$f_e(p) \sim \frac{\gamma p}{\sinh \gamma p} \qquad \gamma^{-1} = 90 \text{ MeV/c} \qquad (3\text{-}6)$$

and an average separation energy $\bar{\varepsilon}$ = 40 MeV. This was found to provide a good fit to proton-nucleus backscattering data in the single-scattering model of Fig. 5 (Amado 1976), and therefore may include contributions from final-state interactions. It is also consistent with quasi-elastic electron scattering results. Our results for the inclusive proton and pion spectra at 800 MeV/A bombarding energy using this distribution are compared with experiment (Nagamiya 1977) in Fig. 10. As expected, the best agreement is found in the large momentum regions for the lighter systems. In particular, both the magnitude and shape of the proton spectra for C+C and Ne+NaF are remarkably well reproduced. The proton spectra at back angles in the heavier C+Pb system, and most low-momentum regions of all spectra, are not well reproduced by the model, indicating the presence of multistep, but not necessarily equilibrium, processes. The pion spectra are generally reproduced only roughly by the knockout calculations, although the agreement for the lightest (C+C) system is good. The better success of the knockout model for protons is to be expected, since single hard nucleon-nucleon collisions preferentially populate distinctive kinematic regions of the proton spectrum. In contrast, because the Δ resonance is produced nearly at rest in NN collisions at 800 MeV, the kinematics of knockout pion production cannot serve as a unique signature of this mechanism, and the knockout pions overlap with those produced by multiple collisions. Pion spectra taken at higher

bombarding energies might therefore serve to verify this picture.

It is evident in Fig. 10 that the shape of the calculated spectra is independent of the target or projectile. This is because the size of the system affects the knockout calculations only in the amount of recoil energy carried away by the residual nucleus, so that for nuclei with more than a few nucleons, the effect is small. However, this serves as a definite prediction of the knockout model and is clearly seen in the large P_T decay of the experimental proton spectra (Nagamiya 1979) and in the tendency toward symmetry about half the beam rapidity at large P_T for Ne+Pb in Fig. 1.

It is also instructive to look at the inclusive proton spectra in a global picture. This is conveniently done by plotting contours of constant invariant cross section in rapidity space (P_T vs. y), where the rapidity y is defined by

$$y = \frac{1}{2} \ln\left(\frac{E + p_{||}}{E - p_{||}}\right) \quad , \tag{3-7}$$

and $p_{||}$ is the momentum of the particle parallel to the beam axis. Rapidity has the convenient property of being additive under a Lorentz transformation in the beam direction. That is, if we transform to a frame which has a rapidity y_L with respect to the original frame, the the rapidity y' of an object in this frame with respect to its rapidity y in the original frame is given by

$$y' = y - y_L \quad .$$

Therefore, contours of constant invariant cross section plotted in rapidity space look identical in any frame moving parallel to the beam axis.

In Fig. 11 we compare our calculation with experiment in a rapidity plot for the symmetric system Ne+NaF (Nagamiya 1977). It is apparent that the hard-scattering calculation using f_e (Eq. 3-6) with γ^{-1} = 90 MeV/c decays more rapidly than the data in the central rapidity region at large P_T (the spectra at 70° for C+C in Fig. 10 suggests this also). However, the same calculation with γ^{-1} = 110 MeV/c provides a much better fit to the data. This raises the important question of whether f_e with γ^{-1} = 110 MeV/c instead of γ^{-1} = 90 MeV/c still fits the proton-nucleus backscattering data, in keeping with a consistent parameter-free model.

In making the same comparison for a heavy asymmetric system (such as Ne+Pb of Fig. 1) it is clear that the symmetry about half the beam rapidity of the knockout results does not reproduce the observed asymmetry at low momenta. Therefore, the asymmetry at low momenta for large mass-asymmetric systems appears to be due to effects of the multiple scattering component. Indeed, multiple-scattering calculations do have the correct form (Randrup 1978). However, as previously discussed, the symmetry at large transverse momenta suggests that this region might be dominated by the single-scattering component even for large systems.

We have compared the calculation using the effective momentum distribution $f_e(p)$ described above with two theoretical ground-state momentum distributions derived under differing assumptions. One is the sharp Fermi momentum distribution which is derived for non-interacting Fermions at zero temperature:

$$f_F(p) \sim \begin{cases} 1 & p < 267 \text{ MeV/c} \\ 0 & p > 267 \text{ MeV/c} \end{cases} . \qquad (3\text{-}8)$$

The other is a momentum distribution obtained from many-body exp(S) theory which includes fully two-particle correlations and partially three- and four-particle correlations (Zabolitzky 1978). For ^{16}O the results have been calculated using several different NN interactions. As a rough parametrization of the results for the Reid soft core potential, we use the form

$$f_c(p) \sim \begin{cases} e^{-(\frac{p}{150})^2} & 0 \leq p \leq 344 \text{ MeV/c} \\ 0.0204\ e^{-(\frac{p+203.5}{468.5})^2} & 344 \text{ MeV/c} < p \end{cases} . \qquad (3\text{-}9)$$

In Fig. 12 we compare the three distributions and the fit of Eq. (3-9) for the normalization $\int f(p)p^2dp = 16$. It is seen that the theoretical exp(S) result, $f_c(p)$, has about the same exponential falloff at large momentum as the effective distribution $f_e(p)$, but differs significantly in shape at lower momentum. The normalization of the high-momentum tail is also appreciably lower. However, variations of greater magnitude in the normalization of the high-momentum tail result with differing NN potentials suggest that this is not a well determined quantity.

In Fig. 13 we compare the results of these three momentum distributions for 800 MeV/A bombarding energy. The normalization is for the C+C system but the relative results are, of course, independent of the system size for moderately sized nuclei. As expected, the lower normalization in the high-momentum tail for f_c shows up in a corresponding lowering of the spectra in the high momentum regions (but with the same slope). However, because of the variations in the normalization of the large momentum regions of f_c resulting from the use of different forms for

the NN interactions, a definite conclusion cannot be reached as to the quantitative agreement of the theoretical momentum distribution with experiment. It does seem remarkable, though, that apart from this uncertain shift in the normalization of the spectra in the high momentum regions, the theoretical distribution in the hard-scattering model (with no free parameters) reproduces so many features of the spectra. It is also clear in Fig. 13 that the sharp Fermi distribution grossly underestimates the high momentum regions of the data.

3.6 Summary

In this chapter we have seen that a hard scattering approach can quantitatively describe the high-momentum regions of the inclusive proton spectra. The best agreement with experiment is obtained with an "effective" momentum distribution of the form of Eq. (3-6) which was used to describe proton-nucleus backscattering data (Amado 1976). To within the uncertainties of its calculation, a theoretical momentum distribution (Zabolitzky 1978) derived from many-body theory for finite nuclei also appears capable of reproducing the observed data. This leaves unresolved the question of the appropriateness of using the actual momentum distribution in the basic hard-scattering formula (Eq. 2-7) without including effects of final state interactions (Amado 1977).

The agreement with experiment of the hard-scattering calculation is also not unambiguous verification of the single-scattering assumption, since other models with differing assumptions can also reproduce the inclusive proton spectra. The failure of the inclusive single-particle spectra to make a determination here may be due to the averaging effect of these measurements. What is clearly needed are more exclusive

measurements, such as two-particle correlations, to help to distinguish between the various mechanisms.

4. TWO-PROTON CORRELATIONS

4.1 Expected Results

Because of the two-body nature of the single scattering mechanism, correlations are expected between each pair of scattered nucleons. For free nucleon-nucleon scatterings the measurement of the momentum of one nucleon specifies uniquely the final momentum of the other nucleon by momentum conservation. For nucleus-nucleus collisions this correlation is obscured to some degree, even in the framework of the single scattering model, by three effects: the momentum distribution for nucleons in the nucleus, the scattering of other pairs of nucleons in the same collision, and the inelasticity due to pion production. Inclusion of multiple scatterings obscures this effect even more, and finally, the equilibrium models predict no two-nucleon correlations due to the two-body kinematics discussed above. Recently, the experimentalists have made two-proton inclusive measurements and their results are discussed in the next section. Then in Section 4.3 we compare these with the prediction of the hard-scattering model.

4.2 Experimental Results

Two-proton correlation measurements have recently been made for high-energy heavy-ion collisions by Tanihata et al. (1979). Because of the existence of only one spectrometer they were not able to measure directly the two-proton inclusive cross section $[d\sigma(\vec{p}_1,\vec{p}_2)]/(d^3p_1 d^3p_2)$, but with the use of the spectrometer in coincidence with tag counters which triggered on charged particles with energy above a certain cutoff energy, they were able to determine

$$\int_{R(p_c,\theta,\phi)} \frac{d\sigma(\vec{p}_1,\vec{p}_2)}{d^3p_1 d^3p_2} d^3p_2 \quad , \tag{4-1}$$

where the region $R(p_c,\theta,\phi)$ of integration extends over the solid angle centered at θ and ϕ and momentum $p_2 > p_c$ accepted by the counter. They have measured the ratio

$$R(\vec{p}_1) = \frac{\int_{R(p_c,40°,\phi_1+180°)} \frac{d\sigma(\vec{p}_1,\vec{p}_2)}{d^3p_1 d^3p_2} d^3p_2}{\int_{R(p_c,40°,\phi_1+90°)} \frac{d\sigma(\vec{p}_1,\vec{p}_2)}{d^3p_1 d^3p_2} d^3p_2} \quad , \tag{4-2}$$

corresponding to the ratio of events triggered by counters placed at azimuthal angles 90° and 180° from the spectrometer at ϕ_1 and at an angle 40° from the beam direction. In Fig. 14 contours of equal $R(\vec{p}_1)$ are plotted in the nucleon-nucleon center-of-mass system for C+C at 800 MeV/nucleon with p_c = 645 MeV/c. The shaded area represents the region of momentum space accepted by the tag counter, the points at P and T specify the projectile and target momentum respectively, and the dashed circle through P and T denotes the shell populated by free N-N elastic scatterings. The expected quasi-elastic peak is readily seen in the plot. These features are present even for systems as large as Ar+KCl, although for C+Pb no such correlation is seen (see Fig. 14), not necessarily indicating a smaller contribution from single scatterings for this system, since the effect is expected to go as m^{-1}, where m is the mean proton multiplicity for a nucleus-nucleus collision. This will be shown in the next section.

4.3 Correlations from the Hard-Scattering Model

In this section we describe a calculation of the two-proton correlations in the hard-scattering model. A comparison to the experimental results allows an estimate of the single-scattering component of the inclusive proton spectrum. This analysis is similar to the treatment of Tanihata et al. (1979).

We write the proton inclusive cross section as a sum of three terms

$$\frac{d\sigma}{d^3p} = \frac{d\sigma_{pp}}{d^3p} + \frac{d\sigma_{np}}{d^3p} + \frac{d\sigma_b}{d^3p} \quad , \tag{4-3}$$

where $\frac{d\sigma_{pp}}{d^3p}$ and $\frac{d\sigma_{np}}{d^3p}$ are the contributions due to a single proton-proton and proton-neutron scattering, respectively, for which both partners undergo no further scatterings. $\frac{d\sigma_b}{d^3p}$ includes everything else--protons which have undergone more than one collision and protons which have undergone only one collision, but whose partners have suffered multiple collisions. We now assume that only the single proton-proton scatterings contribute to the azimuthal correlations; everything else is only a background to this. Then, given that a proton is detected at p_1 with probability $\frac{1}{\sigma}\frac{d\sigma_{pp}}{d^3p_1}$ (its partner is a proton which does not rescatter), the probability that another proton is detected at $\vec{p}_2$ is proportional to $C(\vec{p}_1,\vec{p}_2) + (m-2)\frac{1}{\sigma}\frac{d\sigma}{d^3p}$, where m is the mean multiplicity of scattered protons from a nucleus-nucleus collision and $C(\vec{p}_1,\vec{p}_2)$ is the probability that the partner to the detected proton at $\vec{p}_1$ scatters to $\vec{p}_2$ with normalization $\int C(\vec{p}_1,\vec{p}_2)d^3p_2 = 1$. Similarly, if a proton is detected at $\vec{p}_1$ with

probability $\frac{1}{\sigma}\frac{d\sigma_{np}}{d^3p_1}$ or $\frac{1}{\sigma}\frac{d\sigma_b}{d^3p_1}$, then the probability that another proton is detected at $\vec{p}_2$ is proportional to $(m-1)\frac{1}{\sigma}\frac{d\sigma}{d^3p_2}$. It is clear under these assumptions that the two-proton inclusive cross section obeys the relation

$$(m-1)\frac{d\sigma}{d^3p_1 d^3p_2} = C(\vec{p}_1,\vec{p}_2)\frac{d\sigma_{pp}}{d^3p_1} + (m-2)\frac{1}{\sigma}\frac{d\sigma_{pp}}{d^3p_1}\frac{d\sigma}{d^3p_2}$$

$$+ (m-1)\frac{1}{\sigma}\frac{d\sigma_{np}}{d^3p_1}\frac{d\sigma}{d^3p_2} + (m-1)\frac{1}{\sigma}\frac{d\sigma_b}{d^3p_1}\frac{d\sigma}{d^3p_2} \quad . \qquad (4\text{-}4)$$

For the case $\frac{d\sigma_{np}}{d^3p} = \frac{d\sigma_{pp}}{d^3p}$ and using the fact that $C(\vec{p}_1,\vec{p}_2)$ is negligible when $\vec{p}_1$ and $\vec{p}_2$ differ by an azimuthal angle of 90°, Eq. (4-2) can be written as

$$R(p_1) - 1 = \frac{\sigma \int_{R(p_c,40^\circ,\Phi_1+180^\circ)} C(\vec{p}_1,\vec{p}_2)d^3p_2}{\int_{R(p_c,40^\circ,\Phi_1+90^\circ)} \frac{d\sigma}{d^3p_2} d^3p_2 \,[(2m-3) + (m-1)F(\vec{p}_1)]} \quad , \qquad (4\text{-}5)$$

where $F(\vec{p}) = \frac{d\sigma_b}{d^3p} \Big/ \frac{d\sigma_{pp}}{d^3p}$. Here the m^{-1} dependence is shown explicitly.

With simple assumptions F can be used to estimate the single-scattering component K, the fraction of protons from a nucleus-nucleus collision which are produced from a single NN scattering. We first assume that both F and K are approximately constant in the range of momentum analyzed. For a given nucleus-nucleus collision, let $N_i/2$ denote the number of initial pairs of nucleons which scatter, let N_f

denote the total number of emitted nucleons (differing from N_i by the rescattering of the initial N_i nucleons with other nucleons in the nuclei), and let P be the probability that a given nucleon from the initial N_i nucleons is emitted with no further scatterings. The ratio K_2 of nucleons from N_i for which both partners of a scattered pair are emitted without rescattering to the total number of emitted nucleons N_f is

$$K_2 = \frac{(d\sigma_{pp}/d^3p) + (d\sigma_{np}/d^3p)}{d\sigma/d^3p} = \frac{P^2 N_i}{N_f}$$

$$= \frac{1}{1 + \frac{1}{2} F} \qquad \text{for} \quad \frac{d\sigma_{pp}}{d^3p} = \frac{d\sigma_{np}}{d^3p} \quad . \tag{4-6}$$

Similarly, the knockout fraction K may be written as

$$K = \frac{PN_i}{N_f} \quad . \tag{4-7}$$

Therefore,

$$K^2 = \frac{N_i}{N_f} \frac{1}{1+\frac{1}{2}F} \quad . \tag{4-8}$$

We can make only a rough estimate of the ratio N_i/N_f, but fortunately the uncertainty in K due to the uncertainty in N_i/N_f is diminished due to the relationship as a square root. We assume that the nucleons in N_i which rescatter, $(1-P)N_i$ of them, do so only once, and that they do not rescatter among themselves. Thus,

$$N_f = PN_i + 2(1-P)N_i = (2-P)\, N_i \quad . \tag{4-9}$$

This value is increased by including further scatterings, but decreased by taking into account that some of the nucleons may rescatter among themselves in the second scattering. This estimate of N_f should be sufficiently accurate for our purposes; a gross inaccuracy is not likely, since the size of N_f is ultimately limited by geometry and the finiteness of the nuclei (an average experimental value of N_f for C+C at 800 MeV/A is 7 (Tanihata 1979)). Equations (4-6), (4-7), and (4-9) yield the following relationship for the knockout fraction:

$$K = \frac{K_2}{4}\left[1 + \left(1 + \frac{8}{K_2}\right)^{1/2}\right] \quad , \tag{4-10}$$

where

$$K_2 = \frac{1}{1 + \frac{1}{2}F} \quad .$$

An estimate of the knockout fraction for a given system is obtained by evaluating Eq. (4-5) in the hard-scattering model and normalizing to the data to determine F.

The correlation function $C(p_1,p_2)$ in Eq. (4-5) may be evaluated easily using the Monte Carlo simulation described in the previous chapter, since one keeps track of both nucleons in each NN scattering. In Fig. 15 we compare with experiment the results of our evaluation of Eq. (4-5) using the momentum distributions f_e and f_c [Eqs. (3-6) and (3-9)] for C+C at 800 MeV/A. For this case, the mean proton multiplicity $m = 3.5$ is an experimental estimate by Tanihata et al. (1979). In this plot the spectrometer is fixed at 40^o, corresponding to a slice through the peak of the contour plot in Fig. 4, and is situated to detect a

proton emitted at 90^{o} in the nucleon-nucleon c.m. system for the case of no Fermi motion. The resulting knockout fraction K for the two distributions is .36 for f_c and .73 for f_e. It is evident that the two forms provide substantially different results in both normalization and shape. This is expected, since the distributions differ so much at lower momenta, where the correlations in Figs. 14 and 15 are most sensitive. A sharp peak in the momentum distribution at p = 0 results in a sharp quasi-elastic peak in the correlations, as seen in Fig. 15 for f_c. In fact, the results for f_c are substantially narrower than experiment. However, a wider Gaussian momentum distribution (mean value $\langle p \rangle$ = 260 MeV/c) can fit the width of the experimental peak as shown in the calculation of Tanihata et al. (1979). The form of the distribution f_e is such that the structure of the quasi-elastic peak appears obscured in Fig. 15, suggesting a deficiency in the shape of f_e at lower momenta, but is nevertheless probably not a reflection of the very large momentum behavior. An analysis of the knockout fraction for f_e is most likely unreliable.

Considering the narrowness of the distribution f_c (our parametrization is even slightly narrower than the actual distribution as seen in Fig. 12) and of the resulting peak in the correlations, the estimate of the single-scattering component of 36% for C+C at 800 MeV/A is probably low. Furthermore, the analysis of the spectra is at 90^{o} in the c.m. system, where the individual NN cross sections are smallest and the contribution from single scatterings is expected to be least. Similar calculations by Tanihata et al. (1979) provide estimates of 30-70% (here the

uncertainty is a result of taking the experimental uncertainties into account) for each of the systems C+C, Ne+NaF, and Ar+KCl at 800 MeV/A --certainly a sizable contribution to the inclusive proton spectrum.

These findings have important implications. First, they tend to substantiate or at least support the basic assumption of the hard-scattering model, that the first single scatterings provide a major contribution to the inclusive proton spectra. Moreover, they point to a serious limitation of the equilibrium models which do not include the single-scattering component nor predict the correlations seen in Figs. 14 and 15. However, this analysis is not sensitive to the very large P_T regions of the spectra and does not determine the single-scattering component in this interesting region.

5. PROTON-NUCLEUS BACKSCATTERING IN A MULTIPLE-COLLISION MODEL

5.1 The Theoretical Models

Recent experimental data (Frankel 1976, Brody 1977) of the 180^{o} scattering of protons from nuclei have stirred up considerable interest among theorists. At stake is the basic understanding of the mechanism for the production of protons in the kinematically forbidden region for the interaction of a proton with a free nucleon. This knowledge may be useful in explaining other systems and regimes such as the large P_T region in nucleus-nucleus collisions, as well as providing information on the internal structure of the nucleus.

Several completely different mechanisms have been proposed. Fujita (1977) has found quantitative agreement with experiment by assuming that the incident proton scatters from a 1-, 2-,..., n-nucleon cluster which does not break up in the collision. The probability P_n for this to occur is a free parameter in the model. The proton-backscattering data can also be explained in a single- or hard-collision model (Amado 1976, Brody 1977, Frankel 1977), if it is assumed that there are high-momentum components in the momentum distribution for nucleons in the nucleus. This form for the momentum distribution has also gained theoretical support from a many-body calculation by Zabolitzky and Ey (1978). As demonstrated in Sec. 3.5, the hard-scattering model can also be extended successfully to the regime of nucleus-nucleus collisions.

Because of the success of the cascade models in describing much of the data from proton-nucleus and nucleus-nucleus collisions, it is natural to investigate the possibility that these energetic backward protons are produced from multiple collisions of the projectile proton with nucleons in the nucleus. The calculation of this quantity has not been made with the standard Monte Carlo cascade approach because of the difficulty of producing these events with such small cross-sections. Kopeliovich (1977) attempts to approximate the equations governing the multiple-collision process analytically, but must invoke numerous approximations, including the restriction to bombarding energies much greater than the nucleon rest mass (E>>m)--of marginal validity for much of the data.

In this chapter we describe our approach to calculate the multiple-scattering component of the inclusive proton spectra at 180^{o}.

5.2 Simple Considerations

In order to understand better the kinematics involved in the large-angle production of protons from multiple scatterings, we look at the kinematical boundaries for a nucleon incident on a nucleus with no Fermi motion. We denote the lab energy and momentum of the particle after the ith interaction as E_i and $\vec{k}_i$. The conservation of four-momentum yields

$$(E_{i-1} + m - E_i)^2 - (\vec{k}_{i-1} - \vec{k}_i)^2 = m^2 \quad ,$$

or

$$\frac{k_i}{m+E_i} = \frac{k_{i-1}}{m+E_{i-1}} \cos\theta_i \quad , \qquad (5\text{-}1)$$

where m is the nucleon mass and θ_i is the scattering angle. The momentum after n scatterings may be written as

$$\frac{k_n}{m+E_n} = \frac{k_o}{m+E_o} \prod_{i=1}^{n} \cos\theta_i \quad . \tag{5-2}$$

Given that the particle scatters through a total angle Θ from its initial direction, one can find the θ_i such that k_n is a maximum. This may be done by the method of Lagrange multipliers for the constraint $\Theta = \sum_{i=1}^{n} \theta_i$. Therefore we solve the system of equations

$$m=1,n \quad \frac{\partial}{\partial\theta_m}\left[\prod_{i=1}^{n} \cos\theta_i + \lambda(\Theta - \sum_{i=1}^{n} \theta_i)\right] = 0 \quad , \tag{5-3}$$

where $$\Theta = \sum_{i=1}^{n} \theta_i \quad .$$

It is easily seen that a solution is given by $\theta_i = \Theta/n$. That is, each scattering occurs through the same angle. Solving for k_n^{max} from Eq. 5-2 yields (Kopeliovich 1977)

$$k_n^{max} = \frac{2m\frac{k_o}{m+E_o}\cos^n(\Theta/n)}{1 - \left(\frac{k_o}{m+E_o}\right)^2 \cos^{2n}(\Theta/n)} \quad . \tag{5-4}$$

As an example of the application of Eq. 5-4, the maximum possible momentum for a proton with initial energy of 600 MeV undergoing 6 collisions through an angle of 180^o is 407 MeV/c. Fermi motion must therefore play an important role since protons bombarding ^{6}Li easily

produce protons at 180^{o} with momentum larger than 407 MeV/c (see Fig. 16). Note also that for the limit $n \to \infty$ $k^{max} = k_o$, the same as the elastic scattering from a large nucleus.

5.3 Derivation of the Basic Equations

Several basic assumptions are made in the intranuclear cascade model. First, it is assumed that there is sufficient distance between nucleons that the microscopic description of the scattering from a nucleus is that of a succession of independent, single-particle collisions. We are encouraged here by the cumulative successes of this picture for many years in the Glauber approximation (Glauber 1959, Saudinos 1974) and in the Monte Carlo cascade calculations (Chen 1968, Smith 1977, Randrup 1978). This is not to imply that other mechanisms are not more important in certain regimes. Another assumption generally adopted in the various approaches is that off-shell effects are unimportant, and, related to this, is the historical use of the Fermi (or similar) momentum distribution for nucleons in the ground-state nucleus. Certainly, if one includes the high-momentum components in the ground-state momentum distribution, off-shell kinematics are required for energy conservation.

The picture that emerges for a proton-nucleus collision, then, is that of a proton colliding with a sufficiently dilute Fermi gas made up of on-shell, independent particles confined to some spatial dimension. In addition to this, one may include effects of a non-uniform density of particles and of spatial variations in a mean

nuclear potential. We are now in a position to express these ideas quantitatively.

We consider a beam of particles with momentum $\vec{p}_1$ and particle density ρ_1 interacting with a beam of momentum $\vec{p}_2$ and density ρ_2. The Lorentz-invariant interaction probability per unit 4-space is given by (Chen 1968)

$$P = \rho_1 \rho_2 \ v_{12} \sigma_{12} \quad , \tag{5-5}$$

where v_{12} is the relative velocity of the beams and σ_{12} is the total single-particle interaction cross-section. If, now, there are several beams with momentum $\vec{p}_i$, then the interaction probability with beam 1 is

$$P = \rho_1 \sum_i \rho_i \ v_{1i} \sigma_{1i} \quad ,$$

or for a continuous distribution $f(\vec{p})$

$$P = \rho_1 \rho_o \int f(\vec{p}_2) \ v_{12} \sigma_{12} \ d^3p_2 \quad , \tag{5-6}$$

where ρ_o is the total particle density of the beam and $\int f(\vec{p}) \ d^3p = 1$. In a time Δt and volume Δv, the average number of interactions per particle of beam 1 per path length $(v_1 \Delta t)$ traversed is

$$\lambda_1^{-1} \equiv \frac{P \Delta v \Delta t}{(\rho_1 \Delta v)(v_1 \Delta t)} = \frac{\rho_o}{v_1} \int f(\vec{p}_2) v_{12} \sigma_{12} d^3p_2 \tag{5-7}$$

where λ is the mean-free-path. For scattering in a Fermi sea, the mean-free-path is effectively increased due to the Pauli blocking of final states. If the angular distribution for scattering is

$\frac{1}{\sigma_{12}} \frac{d\sigma_{12}}{d\Omega_k}$, then the effective mean-free-path may be written as

$$\lambda_1^{e^{-1}} = \frac{\rho_o}{v_1} \int f(p_2) v_{12} \frac{d\sigma_{12}}{d\Omega_k} Q(k,k') d\Omega_k \, d^3p_2 \quad , \tag{5-8}$$

where k and k' are the final momenta of the scattered nucleons, and Q(k,k') limits the final states to those consistent with the exclusion principle. For a sharp Fermi momentum distribution with Fermi momentum P_F

$$Q(k,k') = \begin{cases} 1 & k > P_F \text{ and } k' > P_F \\ 0 & \text{otherwise} \end{cases} \tag{5-9}$$

The probability dP for a scattering to occur in the path between s and s+ds is

$$dP = \frac{1}{\lambda^e} e^{-s/\lambda^e} ds \quad , \tag{5-10}$$

if it is assumed that a collision occurs at any time with equal probability, independent of the past history. This is of course not strictly true if one takes into account spatial correlations between nucleons in the nucleus, but, again, we are assuming adequate distances between nucleons that collisions occur sequentially, independent of one another.

We now consider a projectile proton of momentum $\vec{k}_o$ striking a nucleus with uniform density ρ at an impact parameter $\vec{b}$. The number

of nucleons emitted from the nucleus with momentum k_n after n collisions can be written as

$$\frac{dN_n(\vec{b})}{d^3k_n} = \int d^3p_1\, d^3k_1 \ldots d^3p_{n-1}\, d^3k_{n-1}\, d^3p_n$$

$$\times \left[\frac{\rho}{v_o} f(p_1)\, v_{p_1 k_o}\, Q(k_1,k_1')\, 2\, \frac{d\sigma^S}{d^3k_1}\right] \ldots \times \left[\frac{\rho}{v_{n-1}} f(p_n)\right.$$

$$\left. v_{p_n k_{n-1}}\, Q(k_n,k_n')\, 2\, \frac{d\sigma^S}{d^3k_n}\right] \left\{ \int_0^{\ell(\vec{b})} ds_o \int_0^{\ell(\vec{r}_o,\vec{k}_1)} ds_1 \ldots \right.$$

$$\left. \int_0^{\ell(\vec{r}_{n-2},\vec{k}_{n-1})} ds_{n-1} \int_{\ell(\vec{r}_{n-1},k_n)}^{\infty} ds_n\, e^{-s_o/\lambda_o^e}\, e^{-s_1/\lambda_1^e} \ldots e^{-s_{n-1}/\lambda_{n-1}^e}\, \frac{1}{\lambda_n^e}\, e^{-s_n/\lambda_n^e} \right\}. \tag{5-11}$$

Here, the notation is as previously described. The spatial integrals s_i run over the path length $\ell(r_{i-1},k_i)$ from the position in the nucleus at $\vec{r}_{i-1}$ in the direction of $\vec{k}_i$ to the boundary of the nucleus. The next $\vec{r}_i$ is then given by $\vec{r}_{i-1} + s_i \frac{\vec{k}_i}{|\vec{k}_i|}$. The final spatial integral

$$\int_{\ell(\vec{r}_{n-1},\vec{k}_n)}^{\infty} ds_n\, \frac{1}{\lambda_n^e}\, e^{-s_n/\lambda_n^e} = e^{-\ell(\vec{r}_{n-1},\vec{k}_n)/\lambda_n^e} \tag{5-12}$$

is the probability that the particle escapes the nucleus from the position $\vec{r}_{n-1}$ in the direction of $\vec{k}_n$ without rescattering. The

factor of 2 in front of each NN cross-section is needed because two particles are produced at each collision, and the label S on the cross-sections signifies that the angular distributions are symmetric in $\cos \theta_{c.m.}$ since we may keep track of either particle in the collision. Without the factor of 2 and the symmetrized cross-sections, Eq. 5-11 is the probability for a projectile of momentum $\vec{k}_o$ striking a nucleus at impact parameter $\vec{b}$ to undergo n collisions and emerge with momentum $\vec{k}_n$. To see this we form the sum

$$P(\vec{b}) = \lim_{n\to\infty} \int d^3k \sum_{i=1}^{n} (\tfrac{1}{2})^i \frac{dN_i(\vec{b})}{d^3k} \quad . \tag{5-13}$$

We cut off the sum at some large value of n and let the final spatial integral s_n extend to 0, (i.e., $\ell(\vec{r}_{n-1},\vec{k}) = 0$ in Eq. 5-11). This may be an arbitrarily small correction for sufficiently large n. This allows the integration over d^3k and d^3p_n to be carried out to yield $\lambda_{n-1}^{-1} e$ from Eq. (5-8). This term added to the $\frac{dN_{n-1}(\vec{b})}{d^3k}$ term extends the integral over s_{n-1} from 0 to ∞. Proceeding in this manner through all n steps we find

$$P(\vec{b}) = 1 - e^{-\ell(\vec{b})} \quad , \tag{5-14}$$

which is simply the probability for an interaction to occur as the projectile transverses the nucleus at impact parameter $\vec{b}$.

The equation for the proton inclusive cross-section may be written as

$$\frac{d\sigma}{d^3k} = \frac{Z}{A} \int d^2b \sum_{i=1}^{\infty} \frac{dN_i(\vec{b})}{d^3k} \quad , \tag{5-15}$$

where the factor Z/A is included because only protons are detected. For this form to be useful, the contributions from higher orders must be negligible so that only the first few terms need be evaluated.

Eq. 5-11 was derived for a uniform nuclear density ρ. One may easily take into account a spatial variation in ρ by allowing the λ_i^e to depend on $\vec{r}_i$ and by adding multiplicative factors to Eq. 5-11 to insure the proper normalization. This equation also does not include effects of reflection or refraction due to variations in the nuclear potential. These are of decreasing importance (but not necessarily negligible) as one extends to the higher momentum regions.

5.4 Description of the Calculation

The integral of Eq. 5-11 is not at all trivial to evaluate. For six collisions this involves an 18-dimensional integral (after the energy conserving delta functions and the last spatial variable are integrated over). This may reflect the fact that there are many "paths" or "histories" leading to the final state, and, in fact, this is actually the case for most values of the final momentum $\vec{k}_n$. A Monte Carlo evaluation of Eq. 5-11 then requires the sampling of

a sufficient number of paths in order to obtain an unbiased estimate of the integral. However, for the exclusive events of proton back-scattering at large momentum, one might expect that there is a rather restricted set of paths to this final state. This is actually demonstrated for no Fermi momentum in Sec. 5.2. Here it is shown that for scattering through an angle θ, all nucleons produced near the kinematic boundary must be deflected near the angle θ/n for each of the n collisions in the nucleus. We extend this idea to the realistic case with Fermi motion and use the method of "importance sampling" described in Appendix A to concentrate the sampling of paths of Eq. 5-11 to those with large momentum transfers and with deflections near θ/n. Because of the restricted set of paths to the final state, a modest Monte Carlo sampling may be adequate for a good approximation to the integral, even for large n.

In the evaluation of Eq. 5-11, we neglect inelasticity due to pion production. This is not negligible for a bombarding energy of 600 MeV, where the inelastic to total cross-section is approximately 1/4. The net effect of the energy loss from pion formation is expected to reduce the calculated cross-sections.

Several integrations in Eq. 5-11 may be done immediately. For elastic scattering, the differential cross-sections $\frac{d\sigma}{d^3k_i}$ in Eq. 5-11 include an energy-conserving delta function. We thus are left

with an angular integral $d\phi_{k_i}$ $d\cos\theta_{k_i}$ (the polar coordinates are in the lab frame and $\vec{k}_{i-1}$ is in the z direction) for each i<n. For i=n, the final momentum $\vec{k}_n$ is fixed, and we absorb the delta function in the integration over the final internal momentum p_n, leaving an angular integral $d\phi_{p_n}$ $d\cos\theta_{p_n}$. In the actual computation of Eq. 5-11, one must solve for k_i in terms of $\vec{k}_{i-1}, \vec{p}_i, \cos\theta_{k_i}$, and ϕ_{p_i} for each i<n and for p_n in terms of $\vec{k}_{n-1}, \vec{k}_n$, $\cos\theta_{p_n}$, and ϕ_{p_n} at the last collision. General equations which do this are derived in Appendix C. The final spatial integral may also be done beforehand yielding Eq. 5-12.

One could now attempt to evaluate Eqs. 5-11 and 5-15 using ordinary Monte Carlo techniques of sampling evenly in each variable of integration and then weighing each event or path by the integrand (see Eqs. A-1 and A-2 in Appendix A). For a sufficiently large sampling, this yields the correct value. However, in most cases this is much too inefficient. We alternatively use the method of "importance sampling", motivated above, to choose the integration variables to maximize the yield in the backward direction. For each variable $\cos\theta_{k_i}$ we multiply and divide the integrand by the function $g(\cos\theta_{k_i})$ which is peaked near $\cos\theta/n$ and make a change of variables to $G(\cos\theta_{k_i})$, where $G(\cos\theta) = \int_{-1}^{\cos\theta} g(x)dx$ (see Eq. A-7).

Similarly, we choose ϕ_{k_i} peaked near 180^o, where the beam direction is at $\phi = 0^o$. We use a form of g which allows flexibility in widths and peak heights. Such a form is

$$g(x) \sim \begin{cases} e^{-\beta^-(a_o - b_o - x)} & x < a_o - b_o \\ 1 & a_o - b_o \leq x \leq a_o + b_o \\ e^{-\beta^+(x - a_o - b_o)} & a_o + b_o < x \end{cases} \tag{5-16}$$

At the end of this section are presented typical values for the parameters a_o, b_o, β^-, and β^+ for the $\cos\theta$ and ϕ variables.

The integration over the internal momentum p_i is done by sampling evenly in each of the variables ϕ_{p_i}, $\cos\theta_{p_i}$, and p_i^3. Alternatively, for a large final momentum, we sometimes choose ϕ_{p_i} from a distribution peaked near ϕ_{k_i} and $\cos\theta_{p_i}$ peaked for negative values. This increases the yield in the backward direction because of the increased number of collisions able to provide large momentum transfers. Similarly, the p_i integral may be weighted for more events close to the Fermi momentum P_F (we are, of course, using the sharp Fermi momentum distribution of Eq. 3-8).

The calculation of the momenta proceeds as follows. $\vec{p}_1$, $\cos\theta_{k_1}$, and ϕ_{k_1} are chosen as described above, with this

specifying k_1. If two solutions of k_1 exist, we choose either solution at random and multiply its weight by two (see Eqs. C-2 and C-5 in Appendix C). We then choose $\vec{p}_2$, $\cos\theta_{k_2}$, and ϕ_{k_2} and so on until we have specified all $\vec{k}_1,\vec{k}_2,\ldots,\vec{k}_{n-1}$. At the final step we choose $\cos\theta_{p_n}$ and ϕ_n and add together the weights for each of the solutions p_n (see Eqs.C-10 and C-11 in Appendix C). If p_n is greater than the Fermi momentum P_F, then the event does not contribute. We generate a set of histories in this manner. Of course, there are many paths which do not contribute and may be thrown out immediately at any step. This occurs if either of the states k_i and k_i' are below the Fermi momentum P_F (a result of the Q factors in Eq. 5-11), if no positive solution k_i exists for a given $\cos\theta_{k_i}$ and ϕ_{k_i}, or if the momentum k_i is less than the final momentum k_n. This last condition follows from the restriction that a particle colliding with a Fermi gas cannot have its energy raised, since this would require a reduction in energy of the target particle, violating the exclusion principle. At the last step the event is thrown out if k_n' is below the Fermi momentum P_F or if the solution p_n for $\cos\theta_{p_n}$ and ϕ_{p_n} is greater than P_F. Once we have arrived as far as the last step, having generated $\vec{k}_1,\vec{k}_2,\ldots,\vec{k}_n$, we sample the $\cos\theta_{p_n}$ and ϕ_{p_n} variables several times to make the procedure more efficient. Perhaps only one percent of the total number of trials will result in a complete history $\vec{k}_1,\vec{k}_2,\ldots\vec{k}_n$. This percentage may vary greatly depending on how restricted the paths are to the final momentum $\vec{k}_n$ and on how peaked the weighting factors are.

Since only a fraction of the trials results in a complete history, we calculate the weighting factors and spatial integrals only after a complete history of momenta has been generated. For each collision we weight with the angular distribution $\frac{1}{\sigma}\frac{d\sigma}{d\Omega_{k_i}}$. Since we make no distinction between protons and neutrons, we choose either of the pp or np angular distributions and total cross-sections at random. In Appendix C we derive equations for $\frac{1}{\sigma}\frac{d\sigma}{d\Omega_{k_i}}\Big|_{lab}$ in terms of its distribution in the c.m. system. The c.m. angular distributions are calculated using the fits in Appendix B.

For each complete trajectory $\vec{k}_1,\vec{k}_2,\ldots\vec{k}_n$, we evaluate the spatial integral in Eq. 5-11 by sampling the integral for between 40 to 150 impact parameters. Consequently, this final computation is accurate enough that no appreciable uncertainties are added to the results. The size of the nucleus plays a role only in the spatial integral, and this allows us to calculate the results for various systems using the same set of kinematic histories. Instead of sampling evenly in the variables $s_o,s_1,\ldots,s_{n-1}$, we first absorb each of the factors e^{-s_i/λ_i^e} into the s_i integrals of Eq. 5-11 to obtain

$$\left\{\right\} = \lambda_o^e\lambda_1^e\ldots\lambda_{n-1}^e \int_{e^{-\ell(\vec{b})/\lambda_o^e}}^{1} d\xi_o \int_{e^{-\ell(\vec{r}_o,\vec{k}_1)/\lambda_1^e}}^{1} d\xi_1 \ldots \int_{e^{-\ell(\vec{r}_{n-2},k_{n-1})/\lambda_{n-1}^e}}^{1} d\xi_{n-1}\; e^{-\ell(\vec{r}_{n-1},\vec{k}_n)/\lambda_n^e}. \tag{5-17}$$

where the $\ell(\vec{r}_{i-1},\vec{k}_i)$ are, as before, the distance from the point $\vec{r}_{i-1}$ to the boundary of the nucleus (with radius 1.2 $A^{1/3}$ fm) in the direction of $\vec{k}_i$, and $\vec{r}_i$ is given by

$$\vec{r}_i = \vec{r}_{i-1} - \lambda_i^e \ell n\, \xi_i \frac{\vec{k}_i}{|\vec{k}_i|} \quad . \tag{5-18}$$

We evaluate this using Monte Carlo integration by sampling evenly in the variable ξ_i. The λ_i^e are calculated beforehand from Eq. 5-8 for discrete steps in the incident momentum, and a linear interpolation is used between points. The λ_i^e are presented in Table 1. A check of the accuracy of this procedure was made by calculating λ^e midway between the momenta in Table 1 and comparing these values with the interpolated values. They were always within 4% of each other.

Having described the method for evaluating Eqs. 5-11 and 5-15, the advantages of this approach over the traditional Monte Carlo simulation calculations are apparent. First, by isolating the contributions from the various number of collisions, we may anticipate the path required by a particle in its deflection into the backward direction with large momentum. This allows us to weight the integral to maximize this occurrence. In contrast to this, in Monte Carlo simulation the scattering angles at each collision are chosen from the forward-peaked NN angular distributions, and this maximizes the yield in the forward direction. Another advantage in our approach

is the separation of the kinematics from the geometry. The results for many targets may be evaluated from only one set of kinematic histories, thus reducing the computational effort.

This approach is not without its disadvantages. We neglect some processes which may be simulated simply. These include the inelasticity due to pion production, and reflection and refraction of the particles due to variations in a mean nuclear potential. Also, correlations cannot be calculated in our approach. Finally, there are dangers associated with the weighting of Eq. 5-11. If the integrals are weighted with distributions that are too narrow, this may hinder a good sampling of important contributions from other paths. Of course, for a large enough sample, the result remains unchanged, but for several small samples most of the results would be below the true value with an occasional result very much greater. This can fortunately be checked to some degree by taking several samples to determine their smoothness. Because of this danger, we generally used the widest distributions consistent with good statistics. As a typical example, for the case of six collisions, adequate results are obtained in the lower momentum range using the following parameters for the weighting function of Eq. 5-16: $a_o = .883$, $b_o = .117$, $\beta^- = 3.$, and $\beta^+ = 1.$ for the $\cos\theta_{k_i}$ variable, and $a_o = 3.14159$, $b_o = .7$, $\beta^- = 1.5$, and $\beta^+ = 1.5$ for the ϕ_{k_i} variable. One may also check for consistency by varying these parameters. Because of the statistical nature of this analysis, these are not foolproof checks,

and a small danger still remains. By comparing results from different runs, we estimate that there may be up to half an order of magnitude uncertainty in cases where it is difficult to get good statistics.

We made several checks of our evaluation of Eq. 5-11. We naturally checked numerically the equations governing the kinematics which are presented in Appendix C. We also made tests of the normalization conditions of Eq. 5-11 by integrating over d^3k_n without the spatial part of the integral.

5.5 Comparison of the Results with Experiment

We used the methods described above to calculate the inclusive proton spectra at 180^o for 600 MeV protons incident on Li, C, Cu, and Ta. The results are compared with experiment (Frankel 1976, Brody 1977) in Figs. 16-19. We evaluated Eqs. 5-11 and 5-15 for final momenta 500., 570., 640., 710., and 780 MeV/C and plotted the contribution for each value n of the number of collisions. Straight lines are drawn between the points to guide the eye. It is seen that the absolute magnitude of the calculated cross-sections is below the experimental values, and that they decay more rapidly than experiment.

There are several reasons to believe that the calculated values are actually an upper bound to a more complete calculation. First, we neglect the energy losses due to pion production. We also assume a uniform particle density in the nucleus. The inclusion of a

diffuse surface should decrease the results presented here because of the increase in the single-scatterings occurring in the surface which is weighted more heavily (as the impact parameter) in the evaluation of the cross-section. Furthermore, the effect of the protons escaping from a mean nuclear potential should decrease their final energies,shifting the calculated points to the left a slight amount. Finally, the assumption of a constant density for all times during a collision may not be valid for small systems. After several scatterings there is a depletion of nucleons in the nuclear matter. Taking into account these points, it appears that the multiple-scattering model is unable to explain the large-momentum data at 180^{o} from proton-nucleus collisions.

There are some interesting systematics which are apparent in Figs. 16-19. First, the contributions from the low-n results drop off more quickly at large momentum than the large-n values. This is expected because the kinematic boundaries occur at lower momenta for the low-n results. Secondly, the large-n contribution is relatively greater for the larger systems. This is a direct consequence of the fact that after several steps in the cascade, fewer of the nucleons have escaped from a large nucleus than from a small one.

The calculated results do explain some of the qualitative features of the data. They yield the correct ratio of normalization for the various targets, and they reproduce the tendency for the

cross-sections to decay slightly less rapidly for the larger systems. This last point is a consequence of the greater large-n contribution for the heavier systems.

In conclusion, it appears that the main features of the inclusive proton spectra at 180^{o} cannot be explained in an intranuclear cascade model with a sharp Fermi momentum distribution. These calculations do not tell us which reaction mechanism is dominant for the backward production of energetic protons nor do they tell us that multiple processes play no role (It may be a combination of multiple scatterings with other mechanisms). However, they do imply the existence of other mechanisms (possibilities are, of course, high-momentum components in the momentum distribution, scattering from clusters, etc.), and these must be investigated thoroughly in future work. These results also suggest that the multiple-scattering mechanism may not be dominant in other kinematically forbidden regions, such as the large P_T regions from nuclear collisions.

6. SUMMARY AND CONCLUSION

The main direction of this thesis is the study of the mechanism in an energetic nuclear collision for producing protons in the region kinematically forbidden for an interaction of a proton with a free target nucleon. We first investigate the possibility that these energetic protons are a direct result of the high-momentum tail in the momentum distribution for nucleons in the nucleus. In Chapter 3 we show that agreement with the inclusive proton spectra is obtained in the hard-collision model for such a distribution. Reasonably good results are obtained with a form for the momentum distribution (f_e of Eq. 3-6 with γ^{-1} = 90 MeV/c) with an exponential decay at large momentum which was previously used to explain proton-nucleus backscattering data (Amado 1976). These results are improved using a decreased decay rate for the distribution at large momentum (γ^{-1} = 110 MeV/C), so that results consistent with the experimental data are obtained over four orders of magnitude in a global plot in rapidity space (Fig. 11). This raises some questions for future investigations. Namely, is this form with γ^{-1} = 110 MeV/C consistent with the proton-nucleus data, and, if not (implying that the momentum distribution of the target nucleus depends on the projectile), what are the underlying reasons for the success of the model? Possibilities are that final state interactions destroy the simple dependence of the calculations on the ground-state momentum distri-

bution (Amado 1977 and Sec. 2.5), or that such a distribution is generated through other processes in the collision itself.

The idea of high-momentum components in the momentum distribution of the ground-state nucleus has strong theoretical support. Zabolitzky and Ey (1978) use the exp(S) form of many body theory to calculate the ground-state momentum distribution f_c. The decay at large momentum is similar to the distribution f_e described above (see Sec. 3.5 and Fig. 12). We also use this form to calculate the inclusive proton spectra from nucleus-nucleus collisions. The spectra at high-momentum are below the experimental data, but decay with about the correct slope. However, there are uncertainties in the calculation of the distribution f_c at large momentum. Variations of comparable magnitude to the discrepancy with experiment occur with differing forms for the nucleon-nucleon potentials, and the non-relativistic treatment may not be adequate in this regime. These considerations leave unresolved the question of using the ground-state momentum distribution directly in Eq. 2-7 without including the effects of final state interactions.

The analysis in Sec. 3.5 with various forms for the momentum distribution demonstrate the value of the hard-scattering model in studying their properties; the calculation is sensitive to both the relative normalization of the high-momentum tail and its decay rate. However, as just pointed out, this may not be a direct measure of the ground-state momentum distribution due to the effects of final

state interactions.

All of the comparisons with the hard-scattering model have assumed that there are no large uncertainties in the evaluation of Eq. 2-7. Nevertheless, a possible source of error is the use of the on-shell experimental cross-sections to approximate the off-shell scattering matrix. An off-shell treatment may be valuable in making detailed comparisons and is worthy of further study.

In Chapter 4 we compare the results of the hard-scattering model to two-proton inclusive measurements. With simple assumptions, this provides an estimate of the single scattering component. This analysis is sensitive to the low-momentum behavior of the momentum distribution and reveals a deficiency in the form of the effective momentum distribution f_e. This distribution is so broad at low momenta that the quasi-elastic peak in the azimuthal correlations does not appear. In contrast to this, the sharply peaked f_c distribution reproduces the expected quasi-elastic peak and results in an estimate for the single-scattering component of 36% for C+C at 800 MeV/A. A similar treatment by Tanihata et al (1979) provides an estimate of 30-70% for each of the systems C+C, Ne + NaF, and Ar +KCl at 800 MeV/A. Since these measurements are made at 90^o in the c.m. system where the NN angular distributions are smallest, these estimates for the single-scattering component are expected to be low. Unfortunately, this analysis is not sensitive to the very high-momentum regions of the spectra and provides no information on the

single-scattering component there.

The fact that the equilibrium models do not include effects from single-scatterings represents a serious deficiency in their makeup, and the application of these models to many systems must be questionable. However, the equilibrium approach may still have its uses in describing systems for which its assumptions have stronger justification. One possibility is the restriction to events characterized by a large multiplicity, suggesting a low impact-parameter collision involving many nucleons. Also, from the analysis of the correlations, it is not clear which mechanism is responsible for producing protons in the kinematically forbidden region. If it is mainly a result of multiple collisions, then the equilibrium approach may still be useful here.

In the last chapter we continue our investigation of the kinematically forbidden region by calculating the multiple-scattering component of the inclusive proton spectra at 180^{o} from proton-nucleus collisions. The cross section is written as a sum of the contributions from protons emitted after the nth step in the cascade. This allows us to anticipate the path that a nucleon follows in scattering 180^{o} and to weight the integral to increase the Monte Carlo sampling along this path. The nucleus is assumed to be a Fermi gas confined to a sphere of uniform density. We neglect effects due to the inelasticity of pion production and to the reflection and refraction of the nucleon from variations in the

nuclear potential. Including these effects and a diffuse density at the surface of the nucleus is expected to decrease the calculated cross-sections. However, the results are already below the experimental values and also decay more rapidly than experiment. This suggests that other reaction mechanisms are present.

In summary, the hard-scattering model is able to reproduce the high-momentum behavior of the inclusive proton spectra from relativistic nuclear collisions if one assumes high-momentum components in the momentum distribution for nucleons in the nucleus. Support of this picture is given by two-proton correlations which exhibit pronounced features due to the kinematics of the single proton-proton interactions and by theoretical calculations of the high momentum form of the ground-state momentum distribution. Though these reactions are certainly often very complex, the hard-scattering model appears to be an important first step in their understanding, and must be investigated thoroughly in future studies of relativistic nuclear collisions. This approach may also prove valuable in the study of the momentum distribution for the nucleons in the nucleus. Finally, the results of the calculation of proton-nucleus backscattering in a multiple collision model with a sharp Fermi momentum distribution fall short of the experimental cross-sections, implying the presence of other reaction mechanisms in this region.

Appendix A

MONTE CARLO METHODS

A.1 Integration

Monte Carlo methods (Hammersley 1964, Stroud 1971) can be used to approximate multiple integrals when the number of dimensions involved makes them intractable with ordinary numerical integration. A rough rule of thumb is that Monte Carlo techniques are better than the trapezoidal rule in three dimensions and better than second order rules (e.g., Simpson's rule) in five dimensions (Hammersley 1964a). However, advanced techniques are available to make the Monte Carlo method even more efficient. In this section we explain some of the basics of Monte Carlo integration.

Suppose we are interested in evaluating the integral

$$\theta(f) = \int_R f(\vec{x})\, dx_1 dx_2 \cdots dx_n \quad , \tag{A-1}$$

where R is a region in the n-dimensional space. This can be thought of as the average of the function $f(\vec{x})$ over R if $\vec{x}$ is considered to be a random variable distributed evenly in R. Therefore, an estimate of θ is given by

$$f_N = \frac{V}{N} \sum_{i=1}^{N} f(\vec{\xi}_i) \quad , \tag{A-2}$$

where V is the n-dimensional volume of R and the $\vec{\xi}_i$ are random numbers chosen evenly in R. If we now think of f_N as a function of N random variables $\vec{\xi}_i$, then its mean $\bar{f}_N$ and standard deviation σ_{f_N} are

$$\overline{f}_N = \int f_N \frac{1}{V^N} d^n\vec{\xi}_1 \cdots d^n\vec{\xi}_N = \theta(f) \tag{A-3}$$

and

$$\sigma^2_{f_N} = \int (f_N - \theta)^2 \frac{1}{V^N} d^n\vec{\xi}_1 \cdots d^n\vec{\xi}_N = \frac{\sigma^2_f}{N} \quad , \tag{A-4}$$

where

$$\sigma^2_f = V\theta(f^2) - \theta^2(f) \quad . \tag{A-5}$$

Therefore, as expected, f_N approximates $\theta(f)$ with a measure of error given by the standard deviation $\sigma_f/\sqrt{N}$.

That the error falls off so slowly with N is one of the major drawbacks of Monte Carlo integration. To get a factor of 10 improvement in accuracy, there must be an increase by a factor of 100 in computation time. However, with a little insight one can often significantly improve the accuracy by choosing the function f so as to reduce the standard deviation σ_f. To see what is necessary we rewrite Eq. (A-5) as

$$\sigma^2_f = \int_a^b [(b-a)f(x) - \theta]^2 \frac{1}{(b-a)} dx \quad , \tag{A-6}$$

where we are restricting ourselves to one dimension for clarity. We therefore want $f(x) \simeq \frac{\theta(f)}{(b-a)}$, or equivalently, $f(x) \simeq$ constant. Equation (A-1) can be written as

$$\theta = \int_a^b \frac{f(x)}{g(x)} g(x)\, dx = \int_0^{G(b)} \frac{f(x)}{g(x)} dG(x) \quad , \tag{A-7}$$

where $G(x) = \int_a^x g(y)\, dy$.

Therefore, if we can find a function g(x) such that $\frac{f(x)}{g(x)}$ is approximately constant over the range (a,b) and which can be integrated analytically, then the error can be greatly reduced. This method is known as "importance sampling" and detailed examples of its use are given in Hammersley (1964). What we are in fact doing is concentrating the sampling to regions that are most important and then compensating for this by weighting with the factor f/g instead of f. There are also many other methods available for reducing the error which will not be included here but are discussed in the literature (Hammersley 1964, Stroud 1971).

A.2 Direct Simulation

Another Monte Carlo method is the direct simulation of a probabilistic problem. Many times a physical situation is so complex that it is difficult to describe in a quantitative or analytical form, but can still be mimicked simply. This may also have the advantage of intuitive clarity without being obscured by mathematical formalism. In the main text we use this technique for a calculation because of these advantages and the ease with which the results can be compared to the experimental results which it directly simulates.

In direct simulation we must choose an event x at random according to a probability distribution P(x), where $1 = \int_a^b P(x)\,dx$. The random numbers* r that we generally have available are distributed evenly in

*These are generally referred to as pseudo-random numbers because, although they satisfy the statistical properties of random numbers, they are usually generated by a deterministic method. Calculations employing sequences of pseudo-random numbers have the advantage of being exactly repeatable.

the interval (0,1). If x is chosen by $x = G^{-1}(r)$, where $G(x) = \int_a^x P(\xi)d\xi$ and r is chosen at random uniformly in the interval (0,1), then x has the desired statistical properties. A problem arises when G(x) cannot be determined analytically. In this case for bounded P(x) a technique known as "von Neumann rejection" is often useful (Hammersley 1964a). One chooses pairs of random numbers r_1, r_2 independently in (0,1) until the following relation is satisfied:

$$r_1 \leq P(a + (b-a)r_2) / P_{max} \quad , \tag{A-8}$$

where P_{max} is the maximum value of P(x) in the interval (a,b). We then use $x = a + (b-a)r_2$, all previous pairs being rejected. Again, x chosen in this way has the correct properties. It is easy to see that von Neumann rejection can be an efficient process for flat distributions. Of course, one can also use ordinary numerical methods to calculate G(x) and its inverse $G^{-1}(r)$, and then store the discrete results in an array for fine steps in r. Caution must, however, be exercised to insure that this is done with sufficient accuracy to result in an unbiased sampling of x.

Appendix B

NUCLEON-NUCLEON CROSS SECTIONS

B.1 Angular Distributions for Proton-Proton Collisions

We present below the parametrizations for the elastic differential cross sections for proton-proton collisions in the c. m. system. E is the laboratory kinetic energy in units of 939 MeV. θ is the c. m. scattering angle.

Energy range (units of 939 MeV)	$\frac{1}{\sigma_{el}} \frac{d\sigma_{el}}{d\cos\theta}$
$0 \leq E \leq 0.135$	0.5 (Isotropic)
$0.135 < E \leq 0.6$	$(a+b\cos^4\theta)/2(a+b/5)$
	where $a = 1.949 - 0.327\ E$
	$b = 9.1\ E^5$
$0.6 < E \leq 1.065$	$(a+b\cos^4\theta)/2(a+b/5)$
	where $a=-20.97+90.52E-117.25E^2+48.02E^3$
	$b=150.03-578.33E+734.67E^2-299.46E^3$
$1.065 < E \leq 6.55$	$A\lvert\cos\theta\rvert^N \quad 0 \leq \theta \leq 30^o,\ 150^o < \theta < 180^o$
	$A\frac{\cos^N(30^o)}{f(30^o)} f(\theta) \quad 30^o \leq \theta \leq 150^o$
	where $N=-9.68+16.89E-4.348E^2+0.4469E^3$
	$f(\theta)=p^2 \exp\{-(2.85\ p\ \sin\theta)^2\}$
	$+ \frac{30.0}{s} \exp\{-5.94\ p\ \sin\theta\}$

and p and s are the c. m. momentum and total c. m. energy squared in units of 939 MeV. A is determined by the normalization.

B.2 Angular Distributions for Proton-Neutron Collisions

The parametrizations for the elastic differential cross sections for proton-neutron collisions in the c. m. system are presented here. E is the kinetic energy in units of 939 MeV of a neutron striking a stationary proton. θ is the scattering angle in the c. m. system.

Energy range (units of 939 MeV)	$\frac{1}{\sigma_{el}}\frac{d\sigma_{el}}{d\cos\theta}$
$0 \leq E \leq 0.015$	.5 (Isotropic)
$0.015 < E \leq 0.2$	$A(d+e\cos^4\theta)$ $0<\theta<90^o$
	$A(a+b\cos^2\theta+c\cos^{14}\theta)$ $90^o<\theta<180^o$

where $a=2.1-0.1624/E+0.04011/E^2-0.0004E^3$

$$b = \begin{cases} 1.57+251.7E-502i.E^2+41192E^3-1.162\times10^5E^4 & 0.015\leq E\leq 0.1879 \\ 0 & 0.1879<E\leq 0.2 \end{cases}$$

$$c = \begin{cases} -41.0E+2978.E^2-33953.E^3+108909.E^4 & 0.0168<E\leq 0.2 \\ 0 & 0.015\leq E\leq 0.0168 \end{cases}$$

$$d = -0.9+.377/E+0.0184/E^2-1.77\times10^{-4}/E^3$$

$$e = 182.9E-1408.8E^2+3066.2E^3$$

and

$$A^{-1} = a+b/3.+c/15.+d+e/5.$$

$0.2 < E \leq 0.62$	$A(e+f\cos^2\theta)$ $0\leq\theta\leq90^o$
	$A(a+b\cos^4\theta+c\cos^{14}\theta+d\cos^{100}\theta)$ $90^o<\theta\leq 180^o$

where $a = -0.5+18.26E-41.64E^2+25.08E^3$

$b = 37.42-227.38E+512.62E^2-380.37E^3$

$c = -4.42+35.43E-78.62E^2+59.52E^3$

$d = 4.0$

$e = 1.32+3.95E-6.71E^2$

$f = 4.19+3.34E-44.86E^2+62.18E^3$

and $A^{-1} = a+b/5.+c/15.+d/101.+e+f/3.$

$0.62 < E \leq 1.065$ $\quad (a+b\cos^4\theta)/2(a+b/5)$

where $a = -20.84+88.88E-114.82E^2+47.08E^3$

$b = 149.74-562.82E+704.13E^2-285.13E^3$

$1.065 < E \leq 6.55$ Same as proton-proton distribution

B.3 Total Interaction Cross Sections for Proton-Proton Collisions

The total interaction cross sections for proton-proton collisions are presented here as a function of E, the lab kinetic energy in MeV.

Energy Range	σ_{tot} (mb)
$0 < E \leq 40.$ MeV	$5.3107+3088.5/E-1174.8/E^2$
$40. < E \leq 310.$	$22.429-11.148/E+93074./E^2$
$310. < E \leq 450.$	$3.5475+0.05331E+887.37/E$
$450. < E \leq 656.$	$-0.42718+0.066505E$
$656. < E \leq 754.$	$21.110+0.033673E$
$754. < E \leq 923.$	$42.038+0.0059172E$

$923 < E \leq 1217$	47.814-0.00034014E
$1217 < E \leq 2200.$	50.994-0.0029532E

B.4 Total Interaction Cross Sections for Neutron-Proton Collisions

The total interaction cross sections for neutron-proton collisions are given below as a function of E, the lab kinetic energy in MeV.

Energy Range	σ_{tot} (mb)
$0 < E \leq 40.$ MeV	$6.9466+9069.2/E-5057.4/E^2$
$40 < E \leq 400$	$27.147+1802.0/E+239380./E^2$
$400. < E \leq 656$	24.506+0.021484E
$656 < E \leq 754$	33.245+0.0081633E
$754 < E \leq 1074$	36.573+0.00375E
$1074 < E \leq 1343$	35.410+0.0048327E
$1343 < E \leq 1685$	38.758+0.0023392E
$1685 < E \leq 2200.$	41.389+0.00077821E

B.5 Total Elastic Cross Sections for Nucleon-Nucleon Collisions

We give below the average of the total elastic proton-proton and proton-neutron cross sections. E is the lab kinetic energy in MeV.

Energy Range	σ_{el} (mb)
$0 < E \leq 300.$ MeV	The average of the proton-proton and proton-neutron total interaction cross sections. See Secs. B.3 and B.4.

$300 < E \leq 630.$	34.5454-0.015152E
$630 < E \leq 1040$	29.6098-0,00731707E
$1040 < E \leq 1380$	28.1177-0.0058824E
$1380 < E \leq 2040$	22.0909-0.00151515E
$2040 < E \leq 2800$	28.3947-0.00460526E

Appendix C

KINEMATICS OF THE CASCADE CALCULATION

Given a nucleon with momentum $\vec{p}_1$ (in the z direction) scattering from a nucleon with momentum $\vec{p}_2$ (specified by polar coordinates $\vec{p}_2$, θ_2, and ϕ_2) through an angle θ from its initial direction and at an azimuthal angle ϕ, we derive an expression for the resulting momentum k_1. The other final state is $\vec{k}_2$. We transform the final energy $E(k_1)$ to the c.m. system (denoted by the primed variables), so that

$$E' = \gamma(E(k_1) - \vec{\beta} \cdot \vec{k}_1) \quad , \tag{C-1}$$

where $\vec{\beta} = \dfrac{\vec{p}_1 + \vec{p}_2}{(E(p_1)+E(p_2))}$ and $\gamma = (1 - \beta^2)^{-\frac{1}{2}}$

We write $\vec{\beta} \cdot \vec{k}_1 = \beta k_1 \cos\psi$ and solve Eq. C-1 for the momentum k_1. Thus,

$$k_1^{\pm} = \frac{-E'\beta\cos\psi \pm \{(E'\beta\cos\psi)^2 - (\beta^2\cos^2\psi - 1)(E'^2 - \gamma^2 m^2)\}^{\frac{1}{2}}}{\gamma(\beta^2\cos^2\psi - 1)} \tag{C-2}$$

where $\cos\psi = \Big[p_1\cos\theta + p_2(\cos\theta_2\cos\theta + \sin\theta_2\sin\theta$

$$\times \cos(\phi_2 - \phi))\Big] / |\vec{p}_1 + \vec{p}_2| \quad ,$$

and m is the nucleon mass. There may be up to two solutions of k_1, for a given θ and ϕ. No solution exists when the quantity in the

square roots is negative. Also, since k_1 is taken to be positive, only positive solutions of Eq. C-2 are used.

We now show how to write $\frac{1}{\sigma}\frac{d\sigma}{d\Omega_{k_1}}\Big|_{lab}$ in terms of the angular distribution $f(\cos\theta_{c.m.})$ in the c.m. system, where

$$\int f(\cos\theta_{c.m.})\, d\cos\theta_{c.m.} = 1 \quad . \tag{C-3}$$

It is convenient to rewrite this in terms of Lorentz invariants as

$$1 = \int \frac{E' f(\cos\theta_{c.m.})\ \delta^4(p_1' + p_2' - k_1' - k_2')}{\pi\, k'} \frac{d^3k_1'}{E(k_1')} \frac{d^3k_2'}{E(k_2')} \quad , \tag{C-4}$$

where, as before, the primed variables denote the c.m. system. Transforming to the lab system and carrying out the d^3k_2 integral, we obtain

$$1 = \int \frac{E' f(\cos\theta_{c.m.})\ \delta(E(\vec{p}_1) + E(\vec{p}_2) - E(\vec{k}_1) - E(\vec{p}_1 + \vec{p}_2 - \vec{k}_1))}{\pi\, k'\, E(\vec{k}_2)} \frac{d^3k_1}{E(k_1)}$$

$$= \int d\cos\theta_{k_1}\, d\phi_{k_1} \frac{1}{\sigma}\frac{d\sigma}{d\Omega_{k_1}}\Big|_{lab} \quad , \tag{C-5}$$

where $\frac{1}{\sigma}\frac{d\sigma}{d\Omega_{k_1}}\Big|_{lab} = \sum_{\pm} \frac{k_1^{\pm 2}\ f(\cos\theta_{c.m.})}{2\pi k'\gamma \left| k_1^{\pm} - E(k_1^{\pm})\ \beta\cos\psi \right|}$,

and the sum is over the positive solutions of Eq. C-2. β, γ, and $\cos\psi$ are as previously defined, and k' is the c.m. momentum.

In the final step of the cascade calculation, it is required to solve for the momentum p_2 given p_1, k_1, $\cos\theta_2$, and ϕ_2. The notation is the same as that given above. We form the invariant

$$s \equiv (p_1 + p_2)^2$$

$$= 2m^2 + 2E(p_1)\, E(p_2) + 2p_1p_2 \cos\theta_2$$

$$= 2m^2 + 2E(p_1^B)\, E(p_2^B) + 2p_1^B p_2^B \cos\theta_2^B \quad ,$$

where the superscript B denotes the Breit frame defined by $\vec{p}_1^B + \vec{k}_1^B = 0$. Therefore,

$$2\vec{p}_1^B + \vec{p}_2^B = \vec{k}_2^B$$

and (C-7)

$$|\vec{p}_2^B| = |\vec{k}_2^B|$$

by momentum and energy conservation. These vector relations yield the result

$$p_1^B = p_2^B \cos\theta_2^B \quad . \tag{C-8}$$

$E(p_2^B)$ can be given by the Lorentz transformation to the Breit frame as

$$E(p_2^B) = \gamma(E(p_2) - \vec{\beta} \cdot \vec{p}_2) \quad , \tag{C-9}$$

where $\vec{\beta} = \dfrac{\vec{p}_1 + \vec{k}_1}{E(p_1)+E(k_1)}$ and $\gamma = (1 - \beta^2)^{-\frac{1}{2}}$.

We plug Eqs. C-8 and C-9 into Eq. C-6 and solve for p_2 to obtain

$$p_2^{\pm} = \left[b\, p_1^{B\,2} \pm a\, \mathrm{sign}(b)\, (p_1^{B\,4} - (a^2-b^2)m^2)^{\frac{1}{2}} \right] \Big/ (a^2-b^2), \qquad \text{(C-10)}$$

where

$$a = (E(k_1) - E(p_1))/2 \quad ,$$

$$b = 1/2\; p_1 \cos\theta_2 - 1/2\; k_1(\cos\theta \cos\theta_2 + \sin\theta \sin\theta_2 \cos(\phi-\phi_2)) \quad ,$$

and

$$p_1^{B\,2} = -\left[(E(p_1) - E(k_1))^2 - (\vec{p}_1 - \vec{k}_1)^2 \right] /4 \quad .$$

p_2^- is a solution to Eq. C-6 only if $a^2 - b^2 > 0$ and $a < 0$. There is no solution if $a^2 - b^2$ and $a > 0$, or if the term in the square root is negative.

We also present here an equation for $\int dp_n \left.\dfrac{d\sigma}{d^3k_n}\right|_{lab}$, which is required in the final step of the cascade calculation. Referring to Eq. C-5 we write

$$\int dp_2 \left.\frac{d\sigma}{d^3k_1}\right|_{lab} = \int \frac{dp_n\; E'\; f(\cos\theta_{c.m.})}{\pi\; k'\; E(\vec{k}_2)\; E(\vec{k}_1)}\; \delta(E(\vec{p}_1)+E(\vec{p}_2)-E(\vec{k}_1)-E(\vec{p}_1+\vec{p}_2-\vec{k}_1))$$

$$= \sum_{\pm} \frac{E'\; f(\cos\theta_{c.m.})}{\pi\; k'\; E(k_1) \left| 2b + p_2^{\pm} \left(1 - \dfrac{E(k_2)}{E(p_2^{\pm})} \right) \right|} \quad , \qquad \text{(C-11)}$$

where, again, E' and k' are the c.m. energy and momentum, b is defined in Eq. C-10, and the sum is over all positive solutions of Eq. C-10.

REFERENCES

(Amado 1976) R. D. Amado and R. M. Woloshyn, Phys. Rev. Lett. 36, 1435 (1976).

(Amado 1977) R. D. Amado and R. M. Woloshyn, Phys. Lett. 69B, 400 (1977).

(Amsden 1977) A. A. Amsden, J. N. Ginocchio, F. H. Harlow, J. R. Nix, M. Danos, E. C. Halbert, and R. K. Smith, Phys. Rev. Lett. 38, 1055 (1977).

(Amsden 1977a) A. A. Amsden, F. H. Harlow, and J. R. Nix, Phys. Rev. C 15, 2059 (1977).

(Barish-Schmidt 1973) N. Barish-Schmidt, et al., "Review of Particle Properties," Rev. Mod. Phys. 45 (Supplement) S15 (1973).

(Bjorken 1964) J. D. Bjorken and S. D. Drell, Relativistic Quantum Mechanics (McGraw Hill, 1964), Appendices A and B, pp. 281-290.

(Bjorken 1964a) Ibid, Sec. 8.6, pp. 168-169.

(Bondorf 1976) J. P. Bondorf, H. T. Feldmeier, S. Garpman, and E. C. Habert, Phys. Lett. 65b, 217 (1976).

(Brody 1977) H. Brody, S. Frankel, W. Frati, D. Yang, C. F. Perdrisat, J. Comiso, and K.O.H. Ziock, Phys. Lett. 71B, 79 (1977).

(Chen 1968) K. Chen, Z. Fraenkel, G. Friedlander, J. R. Grover, J. M. Miller, and Y. Shimamoto, Phys. Rev. 166, 949 (1968).

(Frankel 1977) S. Frankel, Phys. Rev. Lett. 38, 1338 (1977).

(Frankel 1976) S. Frankel, W. Frati, O. Van Dyck, R. Werbeck, and V. Highland, Phys. Rev. Lett. 36, 642 (1976).

(Fujita 1977) T. Fujita, Phys. Rev. Lett. 39, 174 (1977).

(Gell-Mann 1951) M. Gell-Mann and F. Low, Phys. Rev. 84, 350 (1951).

(Glauber 1959) R. J. Glauber, Lectures in Theoretical Physics, ed. W. E. Brittin (Interscience, New York, 1959), vol. I, pp. 315-414.

(Gossett 1977) J. Gosset, H. H. Gutbrod, W. G. Meyer, A. M. Poskanzer, A. Sandoval, R. Stock, and G. D. Westfall, Phys. Rev. C 16, 629 (1977).

(Hammersley 1964) J. M. Hammersley and D. C. Handscomb, Monte Carlo Methods (Wiley, New York, 1964).

(Hammersley 1964a) Ibid., Sec. 3.3, p. 35.

(Hammersley 1964b) Ibid., Sec. 3.4, pp. 36-37.

(Hüfner 1977) J. Hüfner and J. Knol, Nucl. Phys. A 290, 460 (1977).

(Koonin 1977) S. E. Koonin, Phys. Rev. Lett. 39, 680 (1977).

(Kopeliovich 1977) V. B. Kopeliovich, Sov. J. Nucl. Phys. 26, 87 (1977).

(Moniz 1971) E. J. Moniz, I. Sick, R. R. Whitney, J. R. Ficenec, R. D. Kephart, and W. P. Trower, Phys. Rev. Lett. 26, 445 (1971).

(Myers 1977) W. D. Myers, "A Model for High Energy Heavy Ion Collisions," LBL-6569 Preprint (August 1977).

(Nagamiya 1977) S. Nagamiya, I. Tanihata, S. Schnetzer, L. Anderson, W. Bruckner, O. Chamberlain, G. Shapiro, and H. Steiner, in Proc. International Conf. on Nuclear Structure, Tokyo, Japan (1977), p. 378, and private communication.

(Papp 1975) J. Papp, J. Jaros, L. Schroeder, J. Staples, H. Steiner, A. Wagner, and J. Wiss, Phys. Rev. Lett. 34, 601 (1975).

(Randrup 1978) J. Randrup, "Proton and Pion Spectra in High-Energy Nuclear Collisions," Preprint (1978).

(Salpeter 1951) E. E. Salpeter and H. A. Bethe, Phys. Rev. 84, 1232 (1951).

(Saudinos 1974) For a review of p-nucleus data: J. Saudinos and C. Wilkin, Ann. Rev. Nucl. Sci. 24, 341 (1974).

(Schmidt 1977) I. A. Schmidt and R. Blankenbecler, Phys. Rev. D 15, 3321 (1977).

(Sivers 1976) D. Sivers, S. J. Brodsky, and R. Blankenbecler, Phys. Rep. 23C, 1 (1976).

(Smith 1977) R. K. Smith and M. Danos, Proc. Meeting on Heavy Ion Collisions, Fall Creek Falls, Tennessee (June 1977); to be published.

(Stroud 1971) A. H. Stroud, Approximate Calculation of Multiple Integrals (Prentice-Hall, Englewood Cliffs, 1971), Ch. 6, pp. 193-216.

(Tanihata 1979) I. Tanihata, M.-C. Lemaire, S. Nagamiya, S. Schnetzer, and H. Steiner, manuscript in preparation (1979).

(Westfall 1976) G. D. Westfall, J. Gosset, P. J. Johansen, A. M. Poskanzer, W. G. Meyer, H. H. Gutbrod, A. Sandoval, R. Stock, Phys. Rev. Lett. 37, 1202 (1976).

(Zabolitzky 1978) J. D. Zabolitzky and W. Ey, Phys. Lett. 76B, 527 (1978).

TABLE 1

The mean-free-path λ and the effective mean-free-path λ^e taking into account Pauli blocking of final states for a nucleon with momentum p (in MeV/c) traversing a Fermi gas with Fermi momentum P_F = 267 MeV/c and density ρ = 0.138 particles/fm^3. These values are calculated from Eqs. 5-7 and 5-8.

p	λ	λ^e
390. MeV/c	1.04 fm	3.53 fm
430.	1.24	3.10
470	1.40	2.85
510.	1.62	3.01
550.	1.73	2.93
590.	1.91	3.10
630.	2.03	3.10
670.	2.09	3.05
710.	2.17	3.07
750.	2.21	3.02
790.	2.23	2.97
830.	2.20	2.86
870.	2.20	2.82
910.	2.16	2.74
950.	2.11	2.65
990.	2.05	2.55
1030.	2.01	2.48
1070.	1.97	2.43
1110.	1.91	2.33
1150.	1.89	2.31
1190.	1.85	2.26
1230.	1.78	2.22
1270.	1.78	2.18

Fig. 1. Contours of constant invariant cross section in rapidity space for the inclusive proton spectra from Ne+Pb at 800 MeV/nucleon (reprinted with permission from (Nagamiya 1977)). y_P and y_T are the projectile and target rapidities, respectively. An interesting feature of this data is the tendency toward symmetry about half the beam rapidity at large P_T. A definition and discussion of rapidity is found in Sec. 3.5. Refer also to Sec. 1.1.

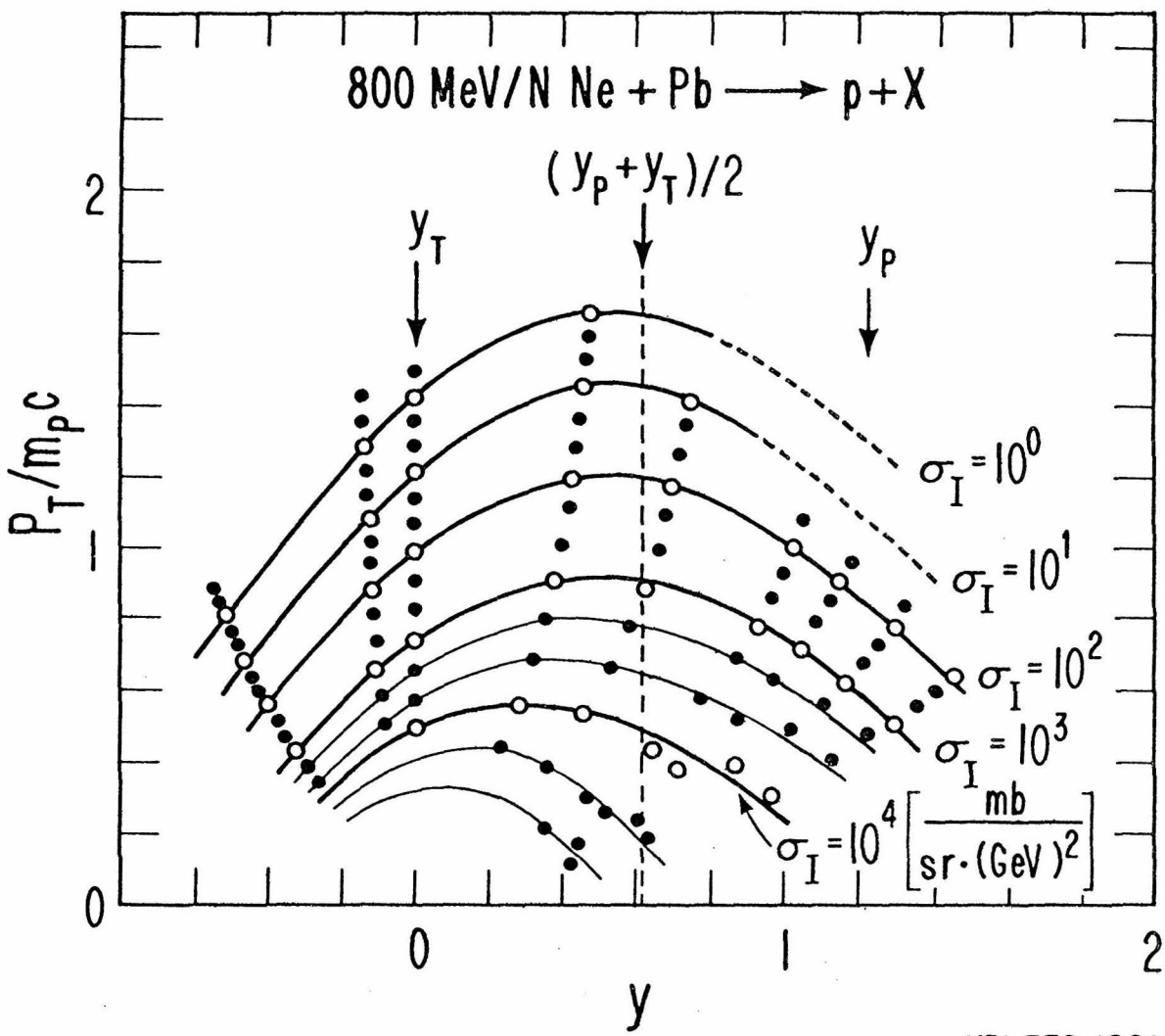
800 MeV/N Ne + Pb ⟶ p+X
(y_P + y_T)/2
y_T
y_P
σ_I = 10^0
σ_I = 10^1
σ_I = 10^2
σ_I = 10^3
σ_I = 10^4 [mb / sr·(GeV)^2]
P_T/m_pc
y
0
1
2
0
1
2

XBL779-1889

Fig. 2. A typical Feynman diagram in quantum electrodynamics. The contribution of the diagram to the wave functions $\Psi^{(A)}$, $\Psi^{(B)}$, and $\bar{\Psi}^{(C)}$ extends from the dashed lines to the ends of the arrows and includes the Fermion propagator at the dashed line. Refer to Sec. 2.1.

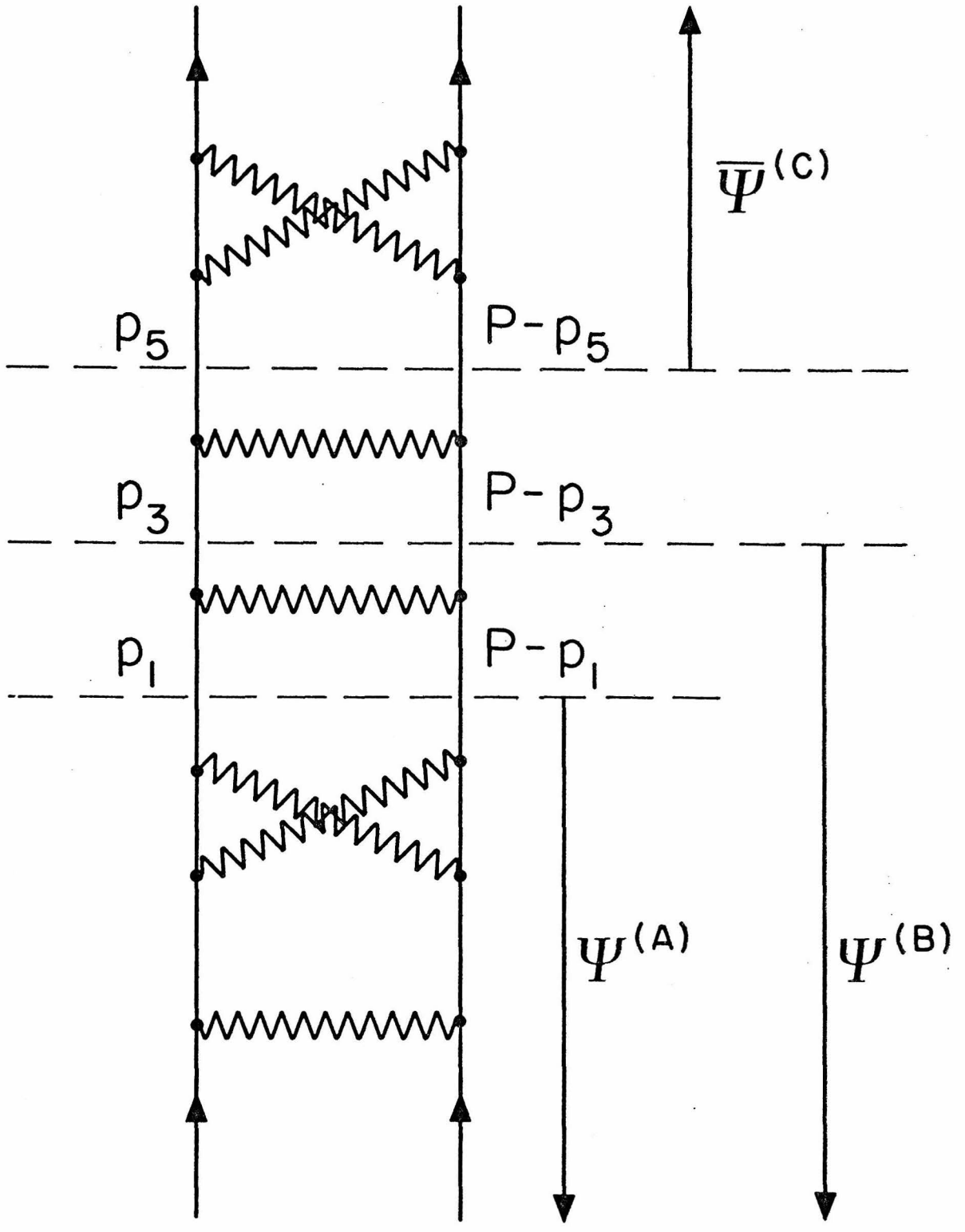
$\overline{\Psi}^{(C)}$
p_5
$P-p_5$
p_3
$P-p_3$
p_1
$P-p_1$
$\Psi^{(A)}$
$\Psi^{(B)}$

Fig. 3. Several of the lowest order irreducible diagrams in QED. Refer to Sec. 2.1.

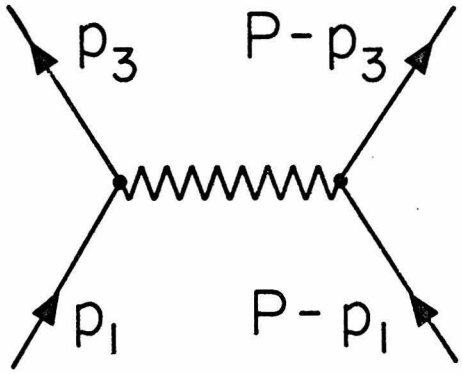

a

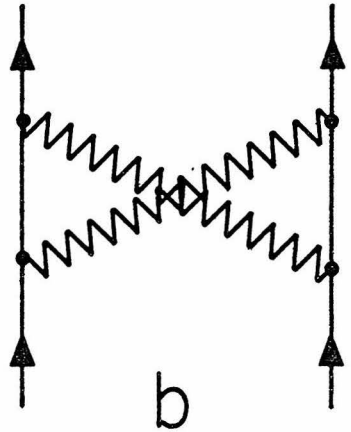

b

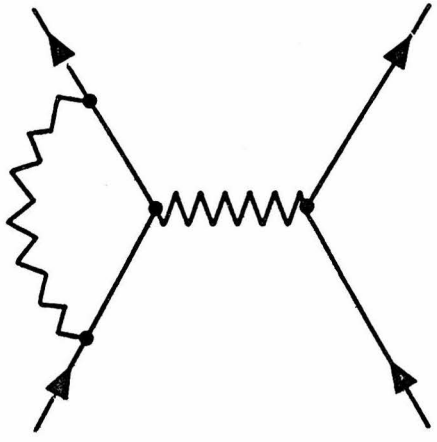

c

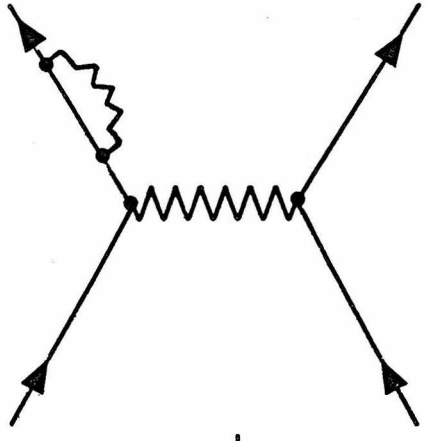

d

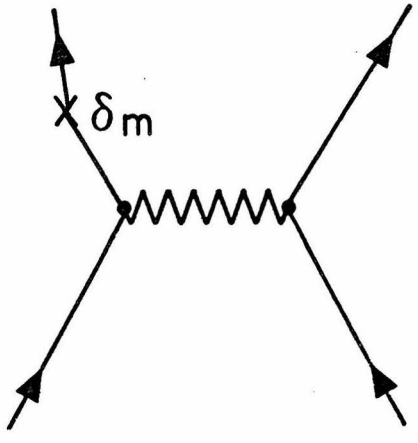

e

Fig. 4. Diagrammatic representation of the hard-scattering mechanism for a nucleus-nucleus collision. Refer to Sec. 2.2.

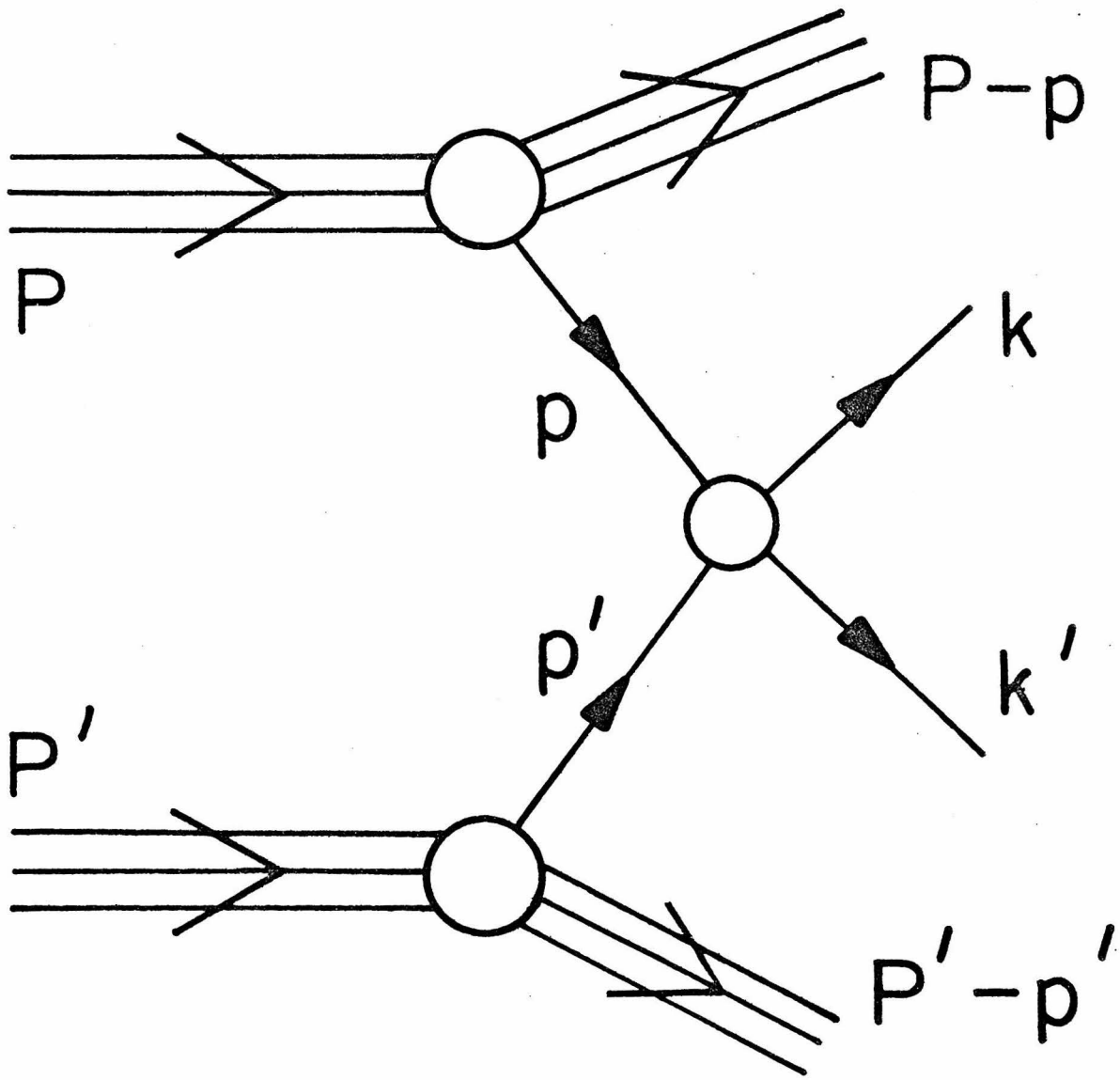
P-p
P
k
p
p′
k′
P′
P′-p′

Fig. 5. The hard-scattering diagram for a proton-nucleus collision. Refer to Sec. 2.2.

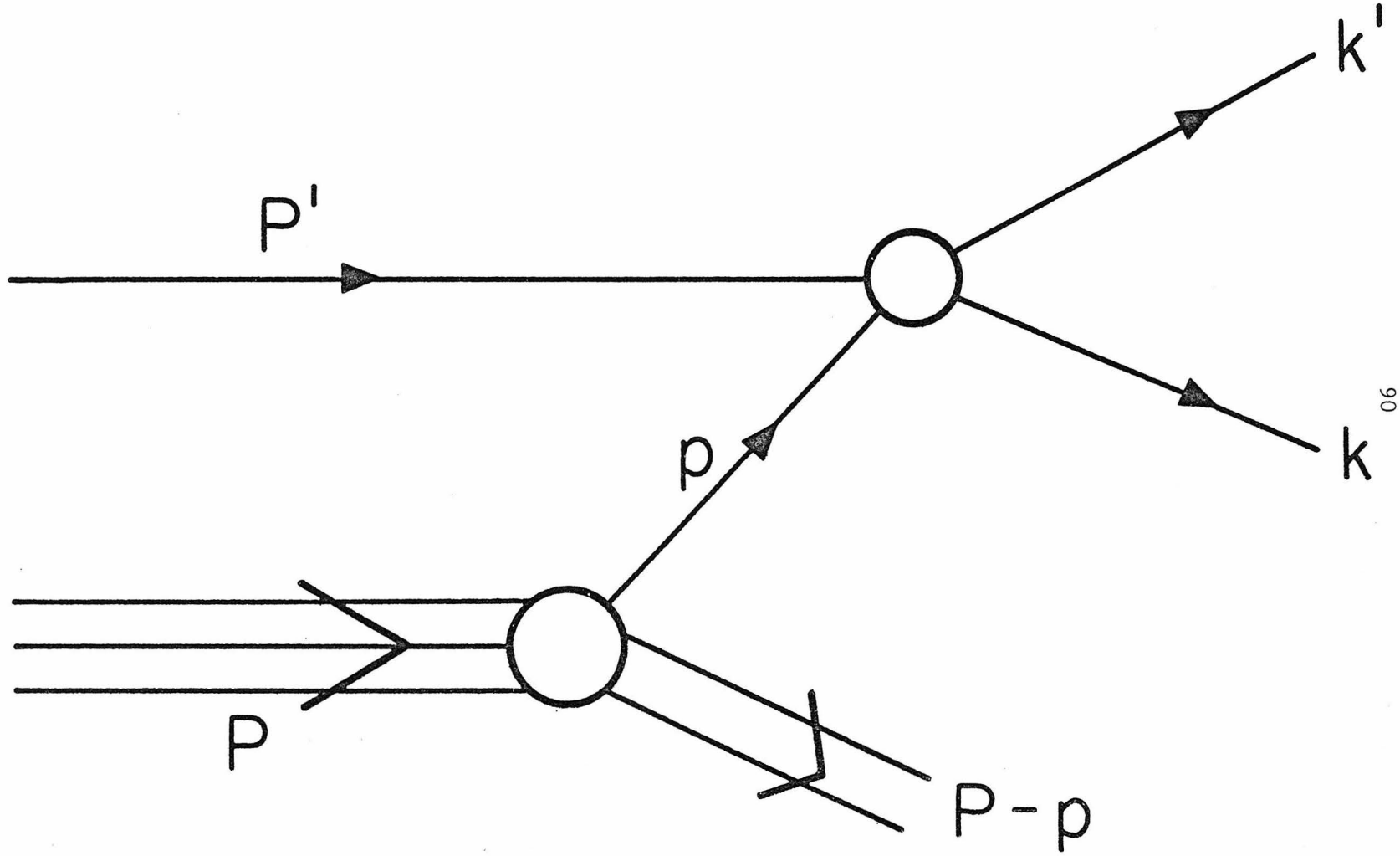
k'
P'
k
p
P
P-p

Fig. 6. The electromagnetic form factor in the impulse approximation showing the kinematics of the Breit frame. Refer to Sec. 2.3.

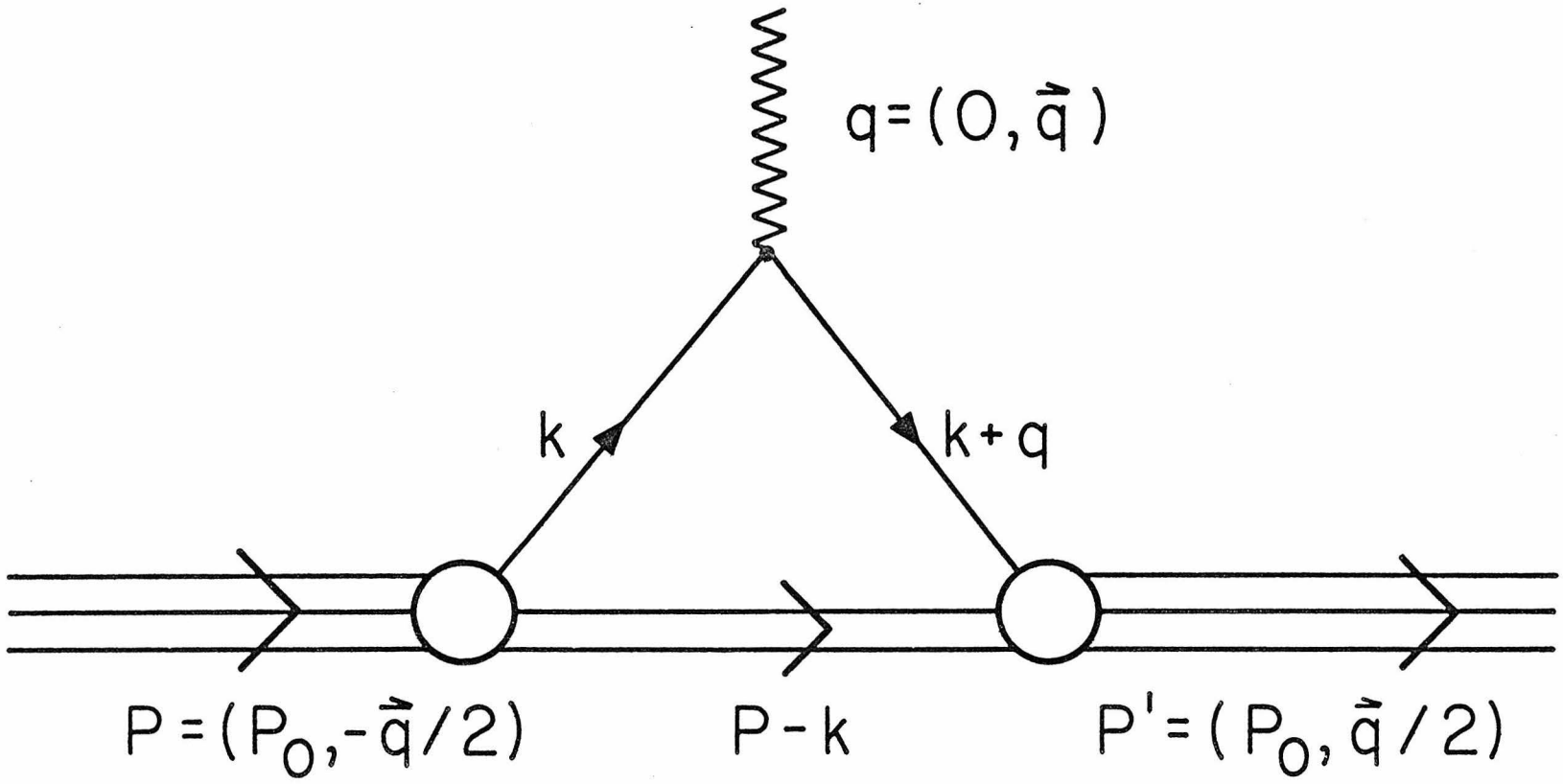
q=(0, q⃗)
k
k+q
P=(P0,-q⃗/2)
P-k
P'=(P0, q⃗/2)

Fig. 7. The diagrammatic representation of the scattering of two pairs of nucleons from a nucleus-nucleus collision. The inclusion of this diagram results essentially in a change in normalization of the results of Fig. 4 and Eq. 2-7. Refer to Sec. 2.4 for a detailed discussion.

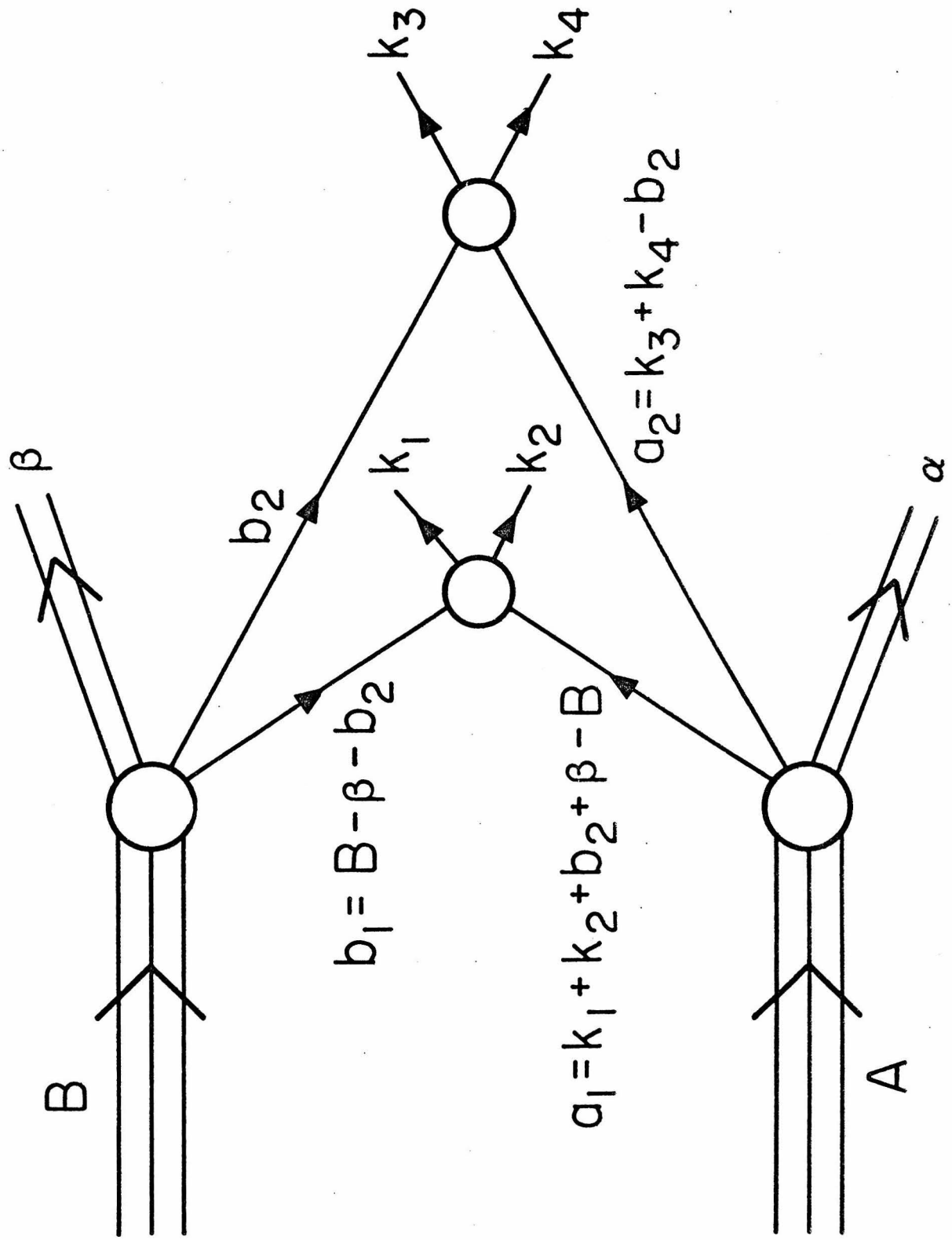
k3
k4
a2=k3+k4-b2
β
b2
k1
k2
α
b1=B-β-b2
a1=k1+k2+b2+β-B
B
A

Fig. 8. A diagram which includes final state interactions. These may play an important role in the scattering process. Refer to Sec. 2.5.

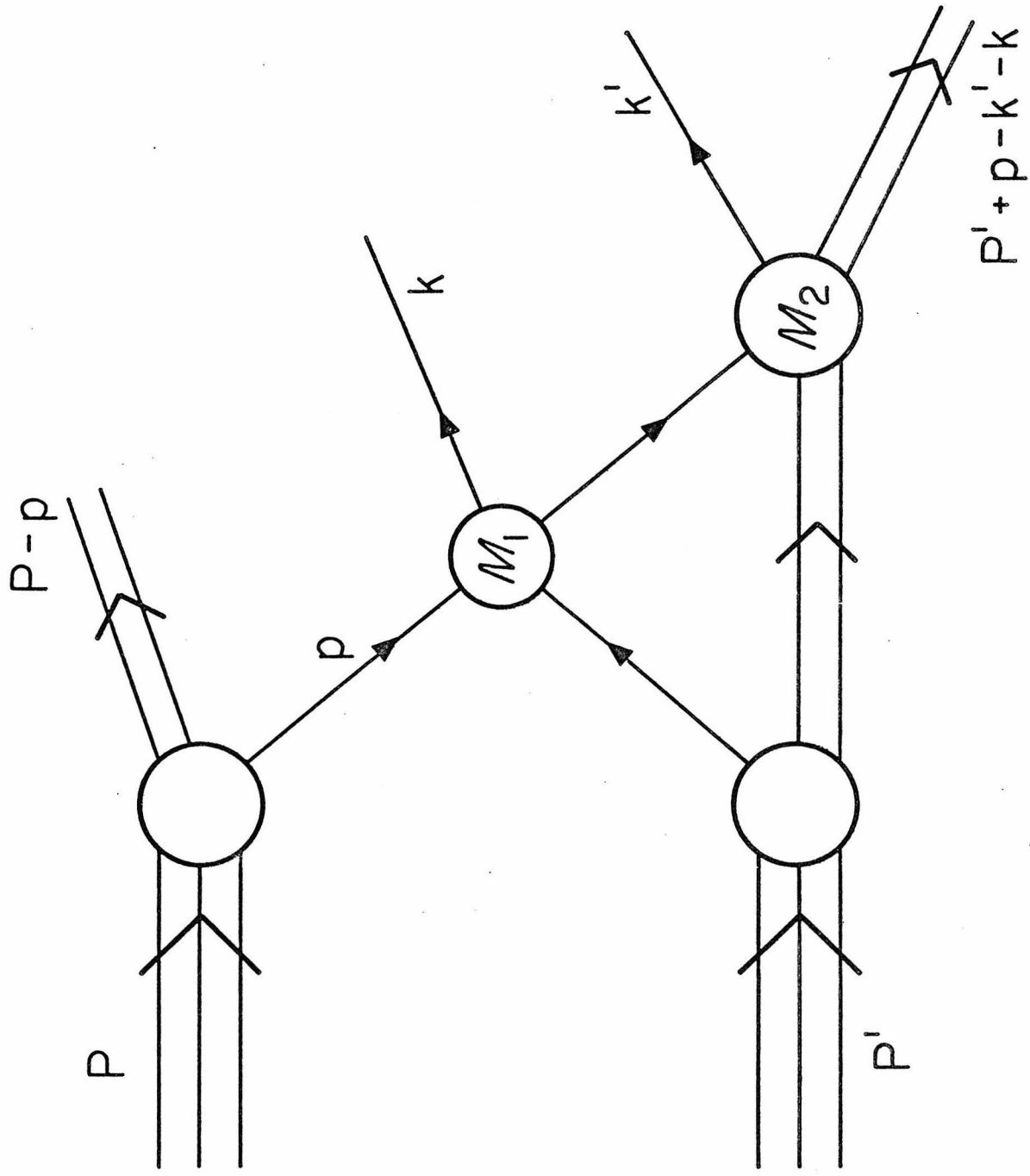
P-p
p
k
k'
P'+p-k'-k
P
P'
M1
M2

Fig. 9. A flow chart of the computer code for the evaluation of Eq. 2-7 with pion production using techniques of Monte Carlo simulation. See Secs. 3.2 and 3.3 for a more complete description.

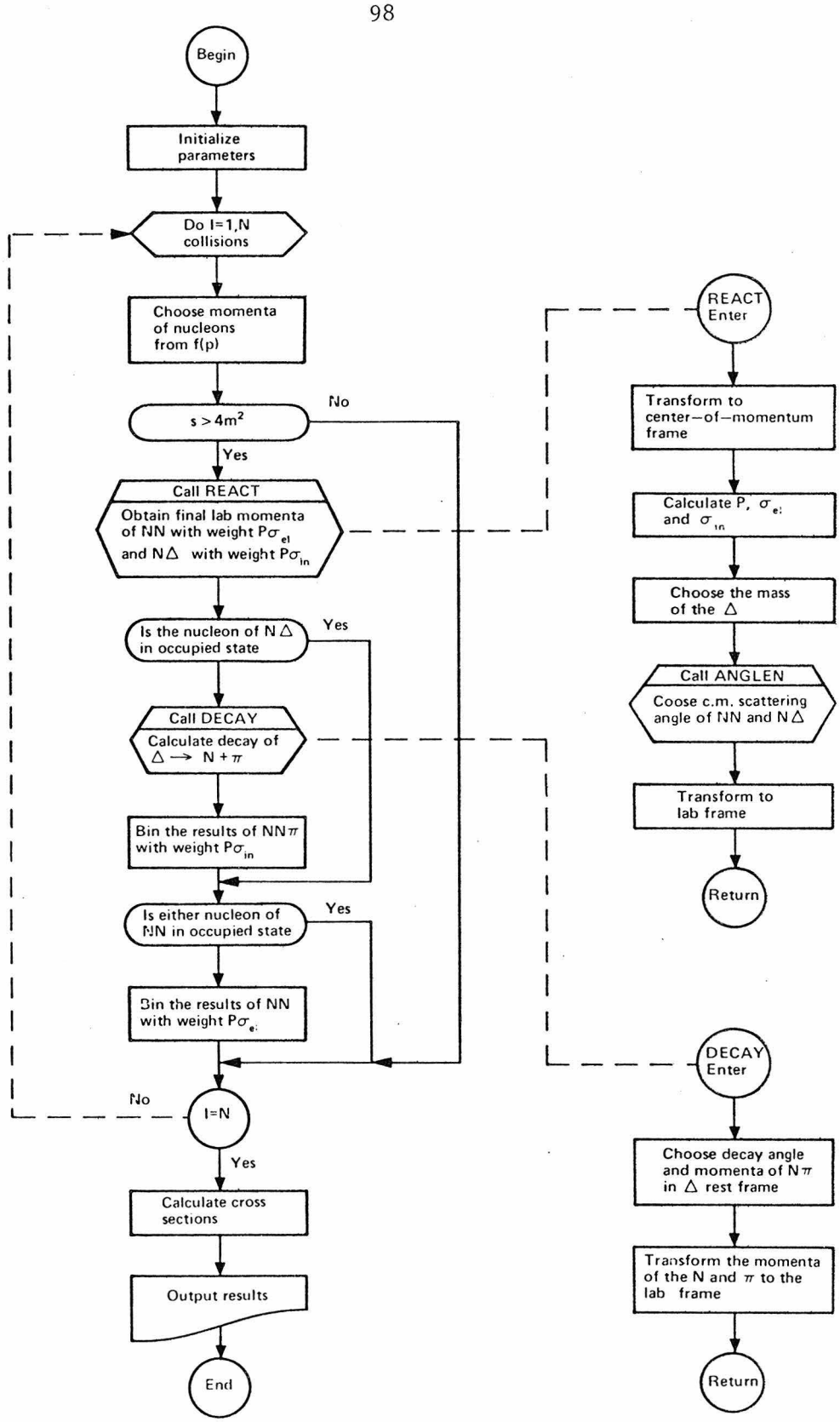
Begin
Initialize parameters
Do I=1,N collisions
Choose momenta of nucleons from f(p)
s > 4m²
No
Yes
Call REACT
Obtain final lab momenta of NN with weight Pσel and NΔ with weight Pσin
Is the nucleon of NΔ in occupied state
Yes
Call DECAY
Calculate decay of Δ → N + π
Bin the results of NNπ with weight Pσin
Is either nucleon of NN in occupied state
Yes
Bin the results of NN with weight Pσel
No
I=N
Yes
Calculate cross sections
Output results
End
REACT Enter
Transform to center-of-momentum frame
Calculate P, σel and σin
Choose the mass of the Δ
Call ANGLEN
Coose c.m. scattering angle of NN and NΔ
Transform to lab frame
Return
DECAY Enter
Choose decay angle and momenta of Nπ in Δ rest frame
Transform the momenta of the N and π to the lab frame
Return

Fig. 10. Comparison of the results of the hard-scattering model using the effective momentum distribution f_e of Eq. 3-6 with experiment for the inclusive proton and pion spectra from collisions at 800 MeV/nucleon. The data of Nagamiya et al (1977) are plotted as functions of the laboratory momentum at various lab angles. Shaded portions of the curves indicate statistical errors in the Monte Carlo evaluation of Eq. 2-7 and arrows indicate the momenta resulting from elastic nucleon-nucleon scattering at 800 MeV. Refer to Sec. 3.5 for a detailed discussion.

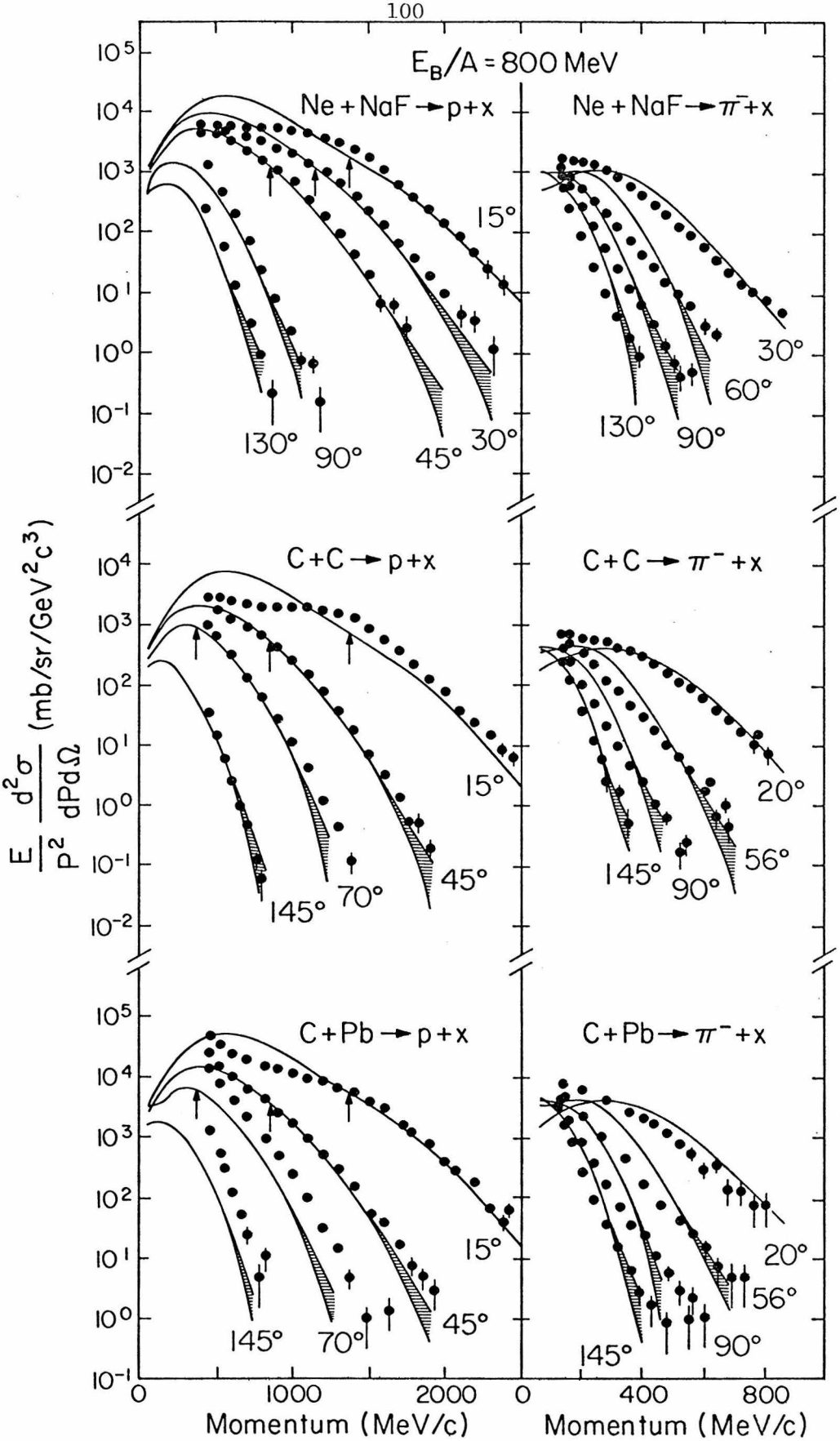
$E_B/A = 800$ MeV
Ne + NaF → p + x
Ne + NaF → π⁻ + x
C + C → p + x
C + C → π⁻ + x
C + Pb → p + x
C + Pb → π⁻ + x
15°
30°
45°
60°
70°
90°
130°
145°
20°
56°
$\frac{E}{P^2}\frac{d^2\sigma}{dPd\Omega}$ (mb/sr/GeV^{2}c^3)
Momentum (MeV/c)
Momentum (MeV/c)

Fig. 11. A comparison with experiment (Nagamiya 1977) of the hard-scattering model in a rapidity plot of the inclusive proton spectra from Ne+NaF at 800 MeV/nucleon. The results are for the effective momentum distribution f_e (Eq. 3-6) with two values of the slope parameter γ. y_P and y_T are the projectile and target rapidities, respectively. The values labeling the curves are the invariant cross sections in (mb/sr/GeV^2 c^3). Refer to Sec. 3.5.

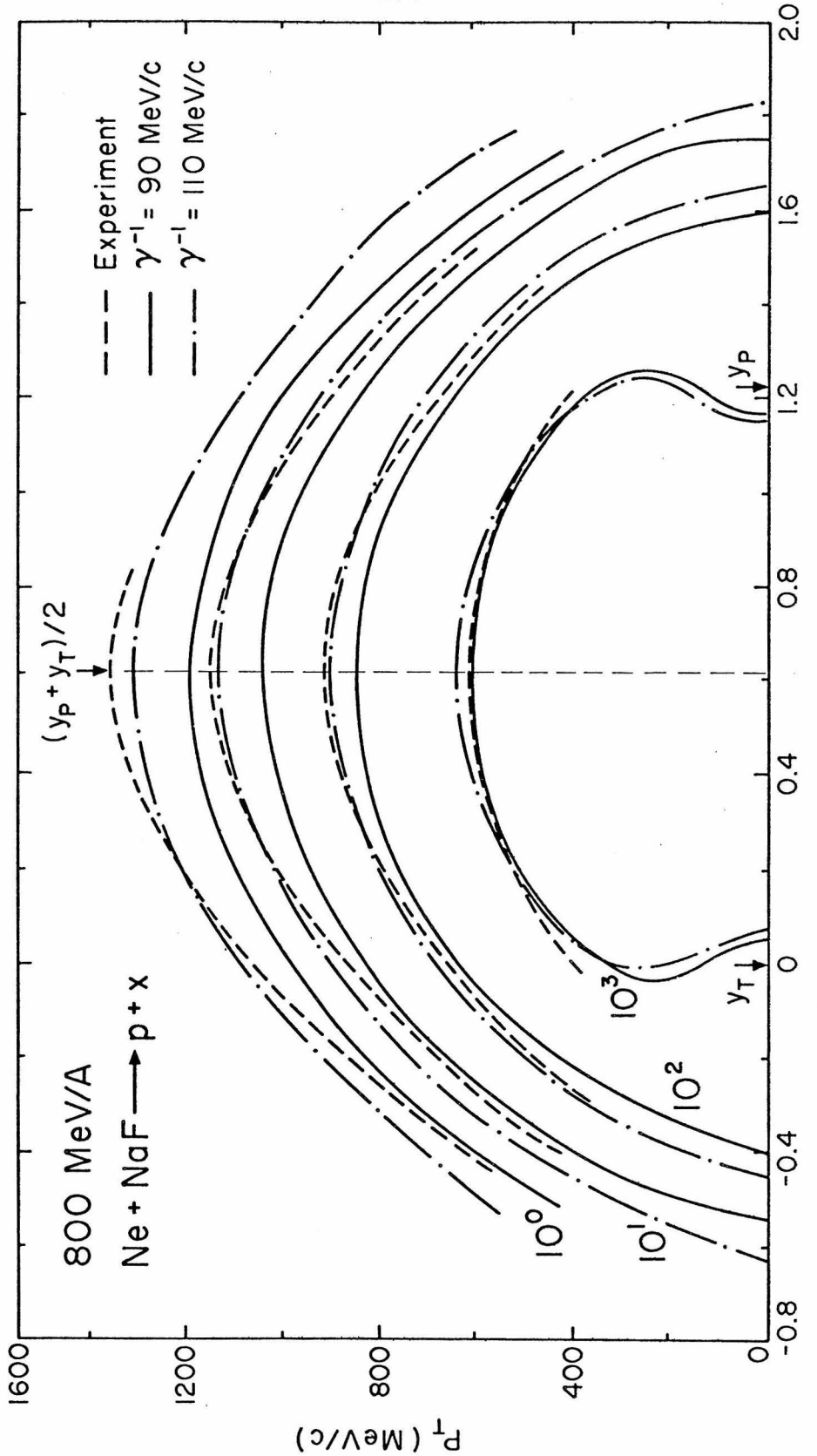
800 MeV/A
Ne + NaF ⟶ p + x
Experiment
γ^{-1} = 90 MeV/c
γ^{-1} = 110 MeV/c
$(y_P + y_T)/2$
y_P
y_T
10^0
10^1
10^2
10^3
P_T (MeV/c)
Rapidity y
1600
1200
800
400
0
-0.8
-0.4
0
0.4
0.8
1.2
1.6
2.0

Fig. 12. A plot of the effective momentum distribution f_e (Eq. 3-6), the sharp Fermi distribution f_F (Eq. 3-8), and the momentum distribution f_c of many-body exp(S) theory (Zabolitzky 1978) for a normalization of $\int f(p)p^2\,dp = 16$. The dashed curve is the fit of Eq. 3-9 to f_c. Refer to Sec. 3.5.

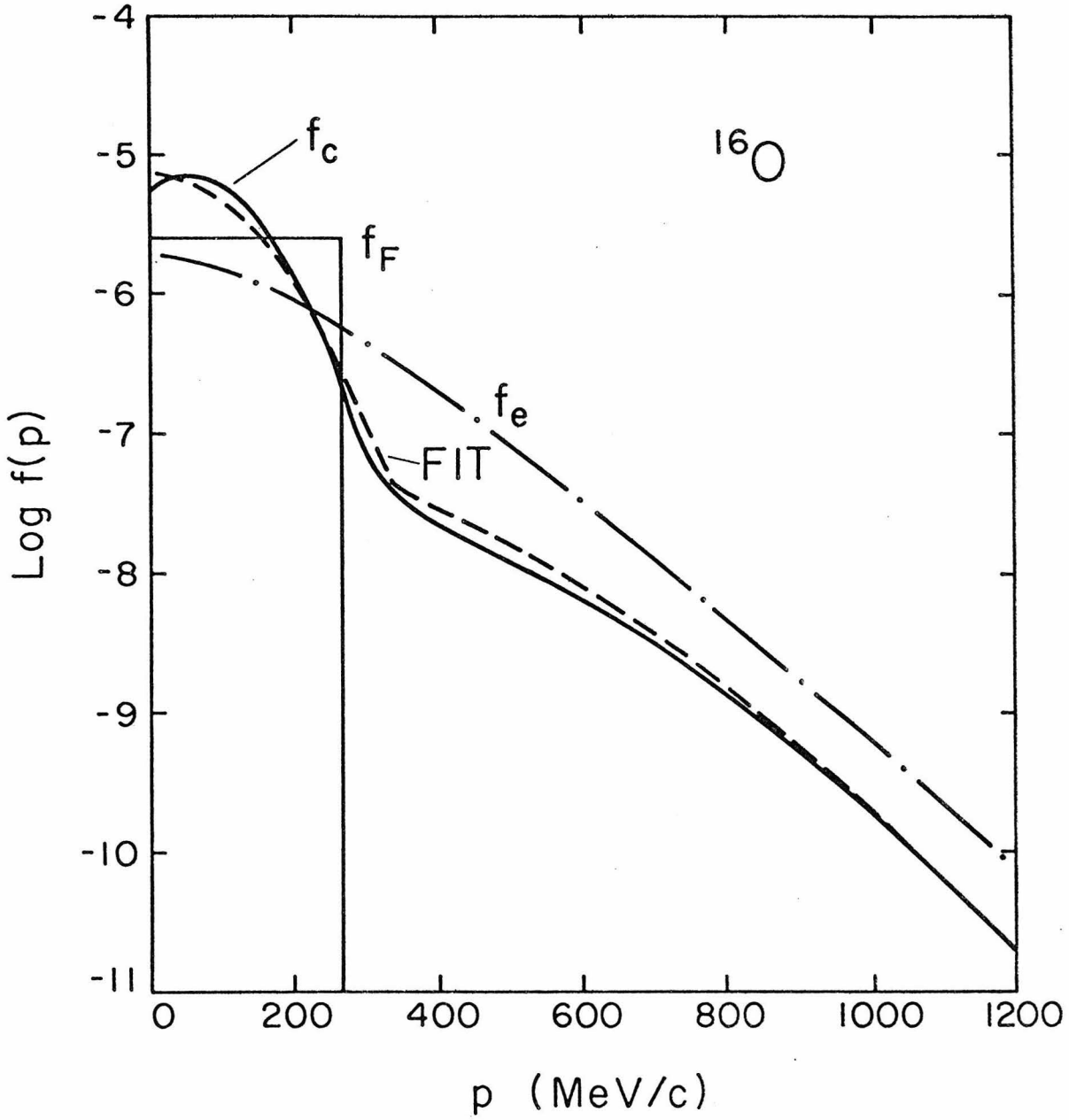
-4
-5
-6
-7
-8
-9
-10
-11
Log f(p)
0
200
400
600
800
1000
1200
p (MeV/c)
f_c
f_F
f_e
FIT
^{16}O

Fig. 13. A comparison of the inclusive proton and pion spectra for the three momentum distributions of Fig. 12 in the hard scattering model for C+C at 800 MeV/nucleon. The results for f_e are also compared with experiment in Fig. 10. Refer to Sec. 3.5.

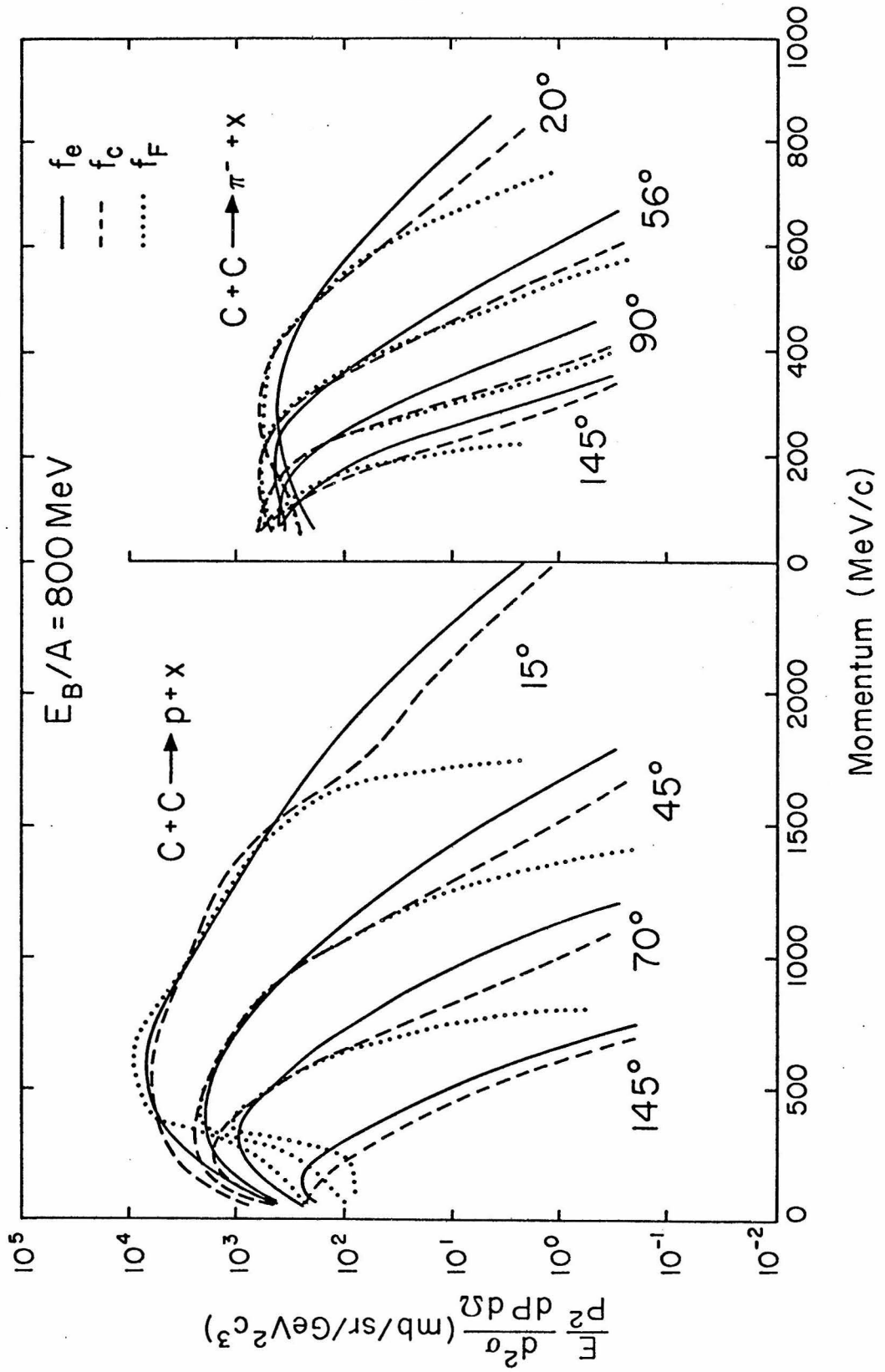
$E_B/A = 800$ MeV
C+C → p+x
C+C → π⁻+x
f_e
f_c
f_F
15°
45°
70°
145°
20°
56°
90°
145°
$\frac{E}{p^2}\frac{d^2\sigma}{dp\,d\Omega}$ (mb/sr/GeV²c³)
Momentum (MeV/c)

Fig. 14. Proton-proton azimuthal correlations by Tanihata et al (1979) for C+C and C+Pb at 800 MeV/nucleon in the c. m. system. The values $R(\vec{p})$ (Eq. 4-2) which label the curves are the ratios of the number of protons detected in coincidence with the trigger at azimuthal angle $\phi=180^{o}$ to those at $\phi=90^{o}$. The shaded area represents the region of momentum space accepted by the trigger, P and T label the projectile and target momenta, respectively, and the dashed circle through P and T denotes the shell populated by free NN elastic scatterings. A strong quasi-elastic peak is seen for C+C but does not appear in the heavier C+Pb system. See Sec. 4.2 for further discussion.

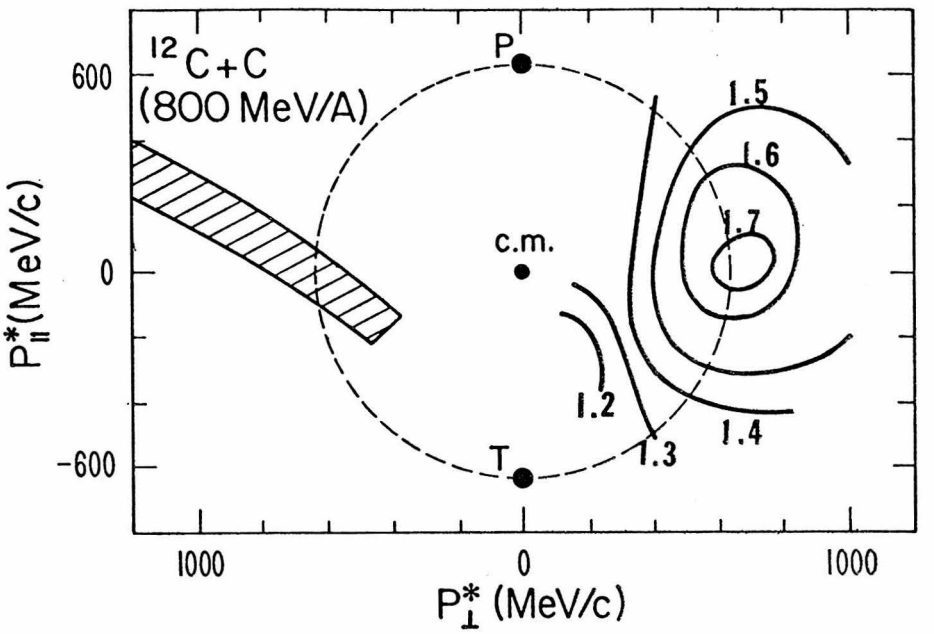
^{12}C+C
(800 MeV/A)
P
T
c.m.
1.5
1.6
1.7
1.2
1.3
1.4
600
0
-600
1000
0
1000
$P_{\parallel}^{*}$(MeV/c)
$P_{\perp}^{*}$ (MeV/c)

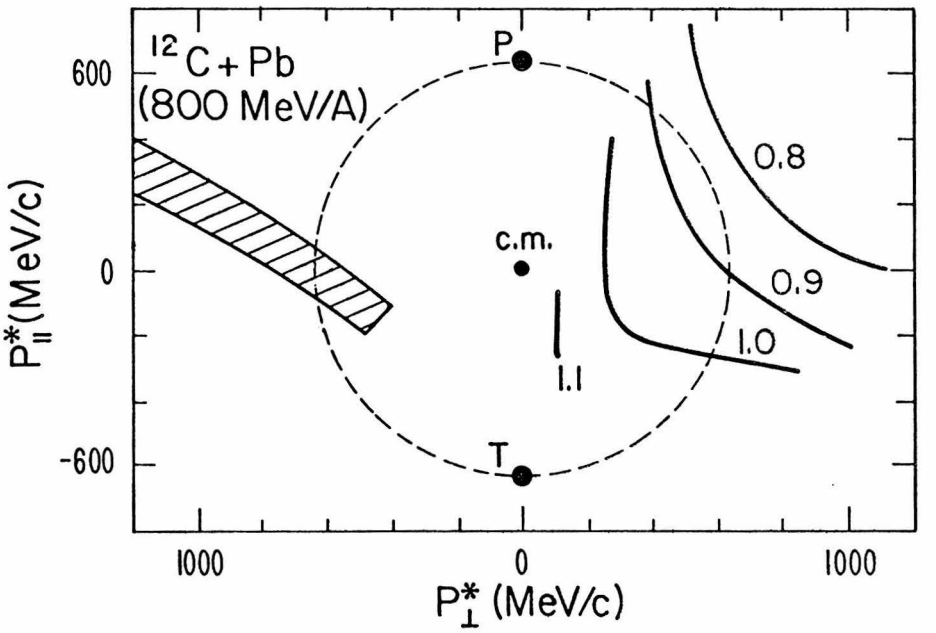
^{12}C+Pb
(800 MeV/A)
P
T
c.m.
0.8
0.9
1.0
1.1
600
0
-600
1000
0
1000
$P_{\parallel}^{*}$(MeV/c)
$P_{\perp}^{*}$ (MeV/c)

XBL 793-758

Fig. 15. Comparison of the hard-scattering model to the experimental results (Tanihata 1979) for the proton-proton azimuthal correlations of C+C at 800 MeV/A. For this plot the spectrometer is fixed at 40^{o} corresponding to a slice through the peak in the contour curves of Fig. 14, and the momentum is in the lab. The theoretical curves are calculated from Eq. 4-5 for the momentum distributions f_e (Eq. 3-6) and f_c (Eq. 3-9). Normalization of these curves to the data allows an estimate of the single-scattering component. Refer to Sec. 4.3 for a discussion of the analysis.

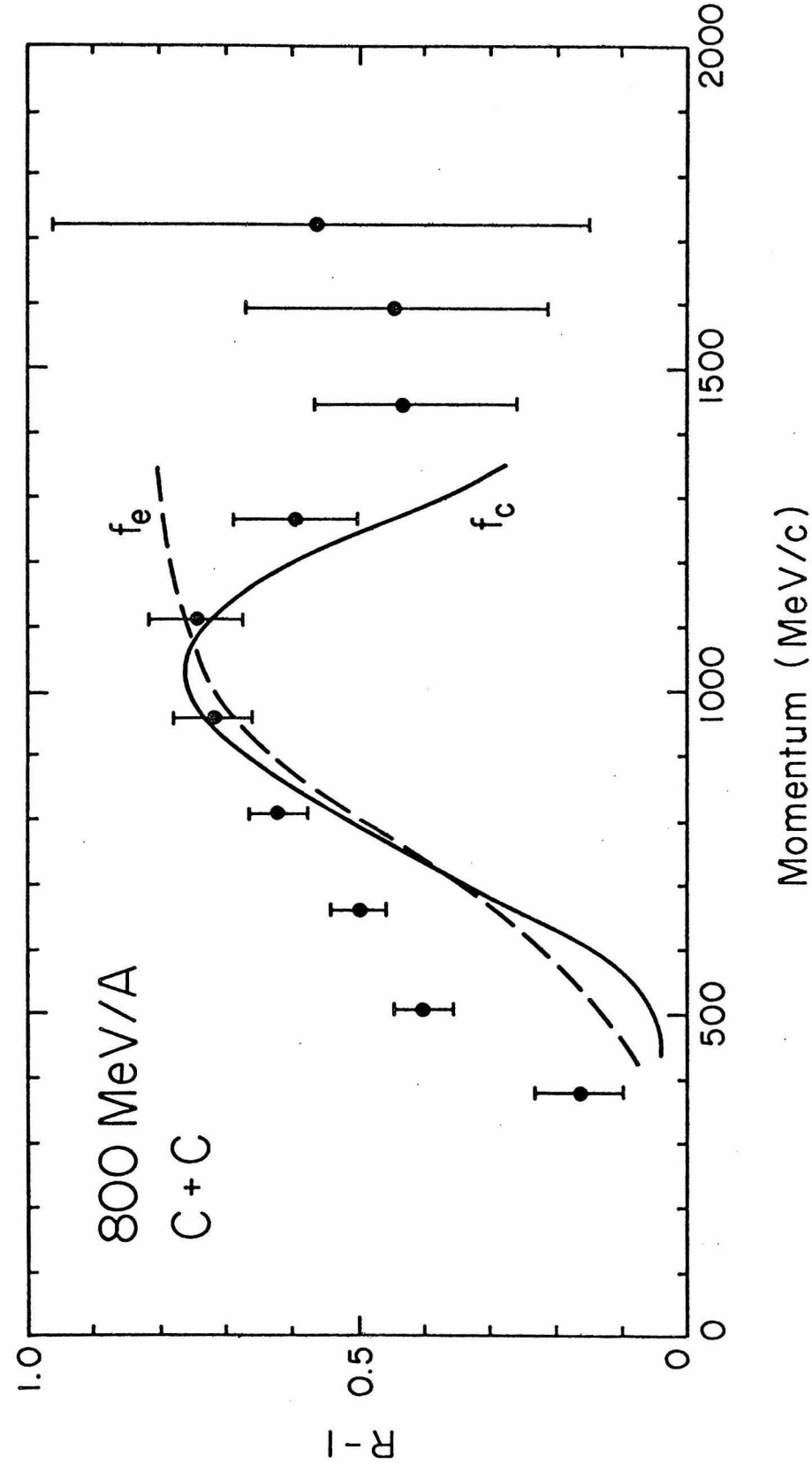
800 MeV/A
C+C
f_e
f_c
R - 1
1.0
0.5
0
0
500
1000
1500
2000
Momentum (MeV/c)

Fig. 16. Comparison with experiment of the results of the multiple collision model for inclusive proton spectra at 180^{o} from p + Li at 600 MeV. The various curves are the contribution to the cross-section from protons emitted after the nth step in the cascade. Straight lines are drawn between the calculated points to guide the eye. The key is: n=3 ·····; 4 —— · ——; 5 —— ——; 6 —— ·· ——; 7 ----; and the total ———. Refer to Sec. 5.5 for a discussion of the results.

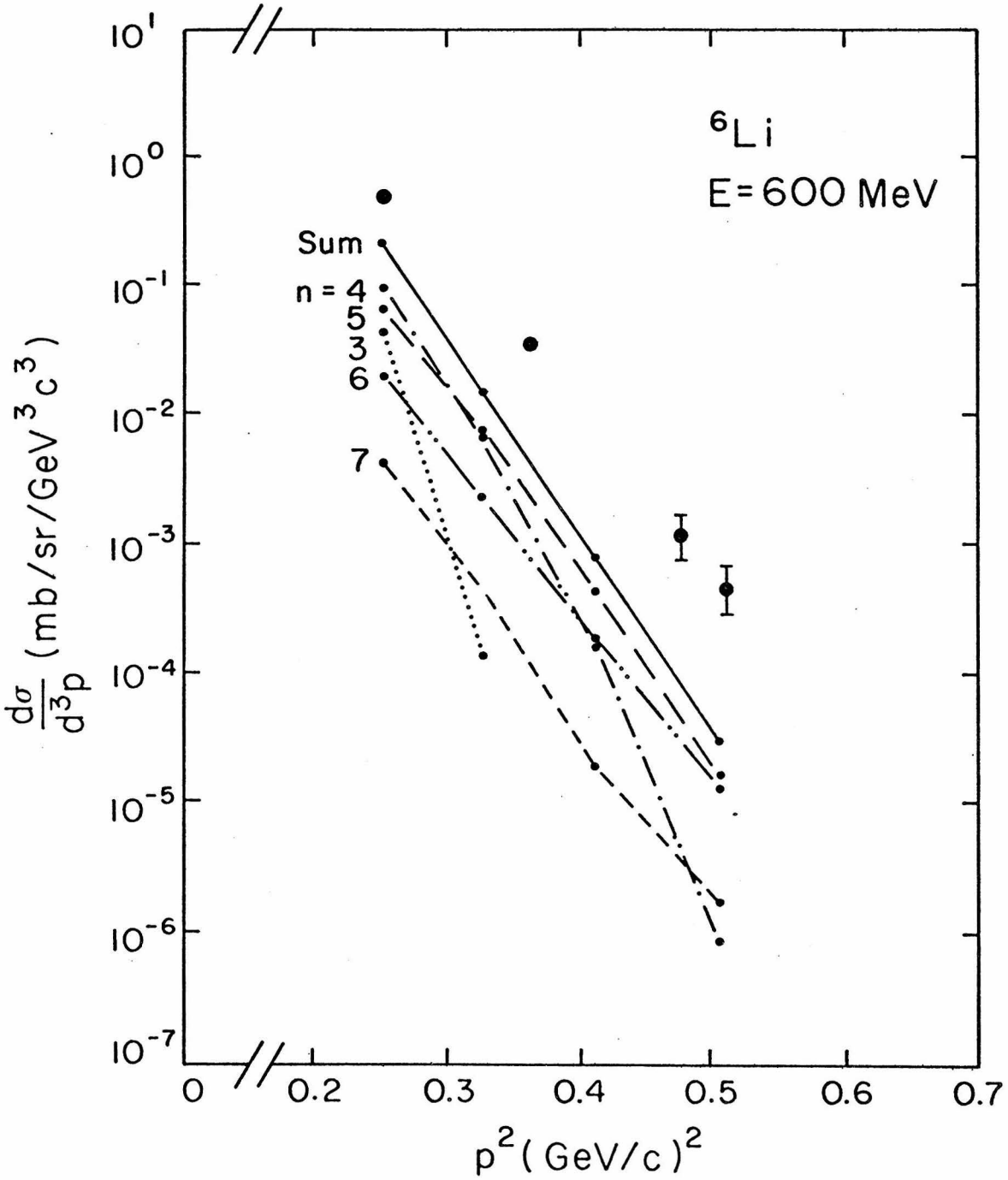
^{6}Li
E=600 MeV
Sum
n = 4
5
3
6
7
$\frac{d\sigma}{d^3p}$ (mb/sr/GeV^{3}c^3)
p^2 (GeV/c)^2
10^1
10^0
10^{-1}
10^{-2}
10^{-3}
10^{-4}
10^{-5}
10^{-6}
10^{-7}
0
0.2
0.3
0.4
0.5
0.6
0.7

Fig. 17. The same as Fig. 16 for p + C. Refer to Sec. 5.5.

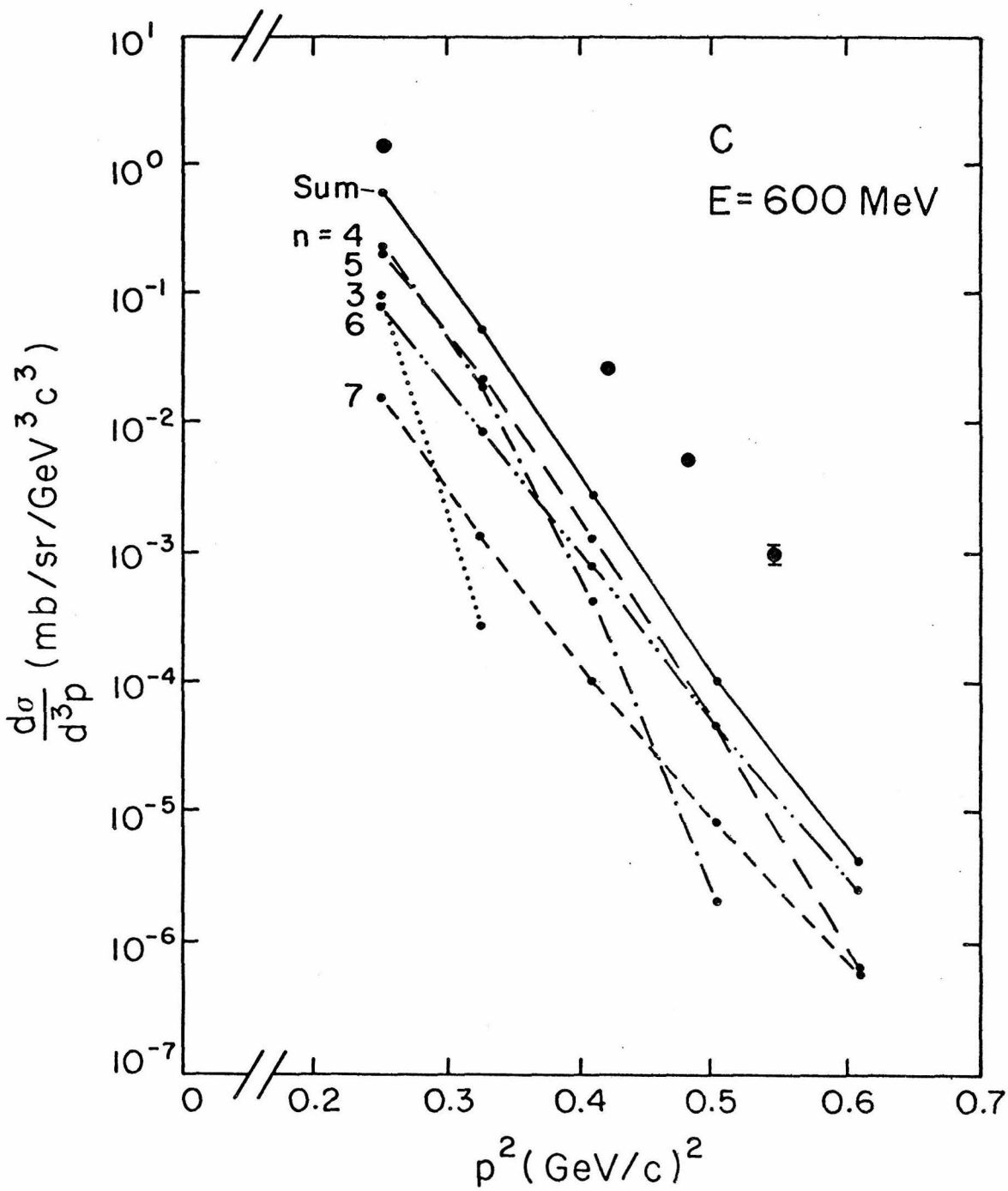
C
E = 600 MeV
Sum
n = 4
5
3
6
7
$\frac{d\sigma}{d^3p}$ (mb/sr/GeV^{3}c^3)
p^2 (GeV/c)^2
10^1
10^0
10^{-1}
10^{-2}
10^{-3}
10^{-4}
10^{-5}
10^{-6}
10^{-7}
0
0.2
0.3
0.4
0.5
0.6
0.7

Fig. 18. The same as Fig. 16 for p + Cu. Here the experimental points are taken from Frankel et al (1976). Refer to Sec. 5.5.

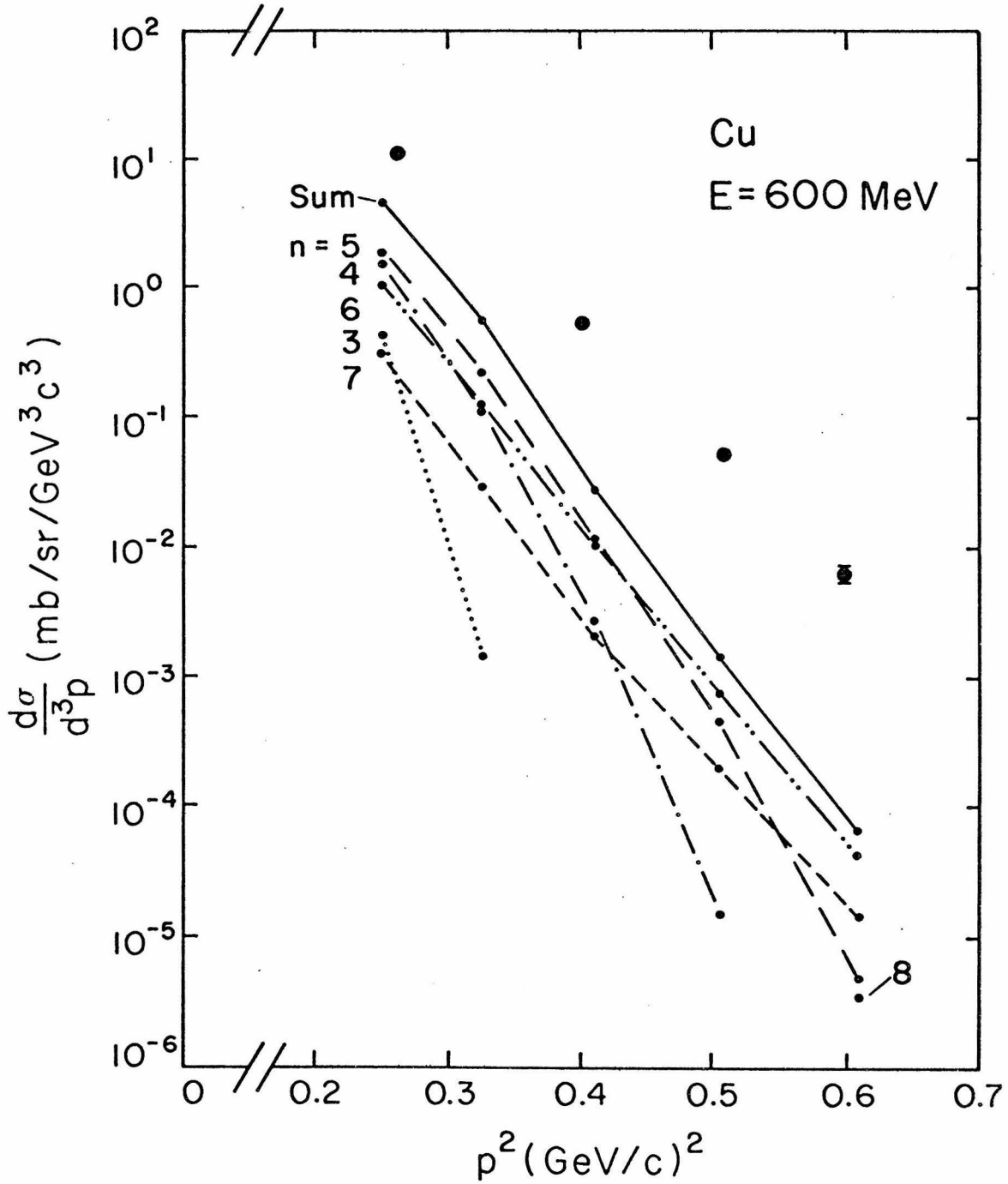
Cu
E = 600 MeV
Sum
n = 5
4
6
3
7
8
$\frac{d\sigma}{d^3p}$ (mb/sr/GeV^{3}c^3)
p^2 (GeV/c)^2
10^2
10^1
10^0
10^{-1}
10^{-2}
10^{-3}
10^{-4}
10^{-5}
10^{-6}
0
0.2
0.3
0.4
0.5
0.6
0.7

Fig. 19. The same as Fig. 16 for p + Ta. The experimental values are taken from Frankel et al (1976) and Brody (1977). Refer to Sec. 5.5.

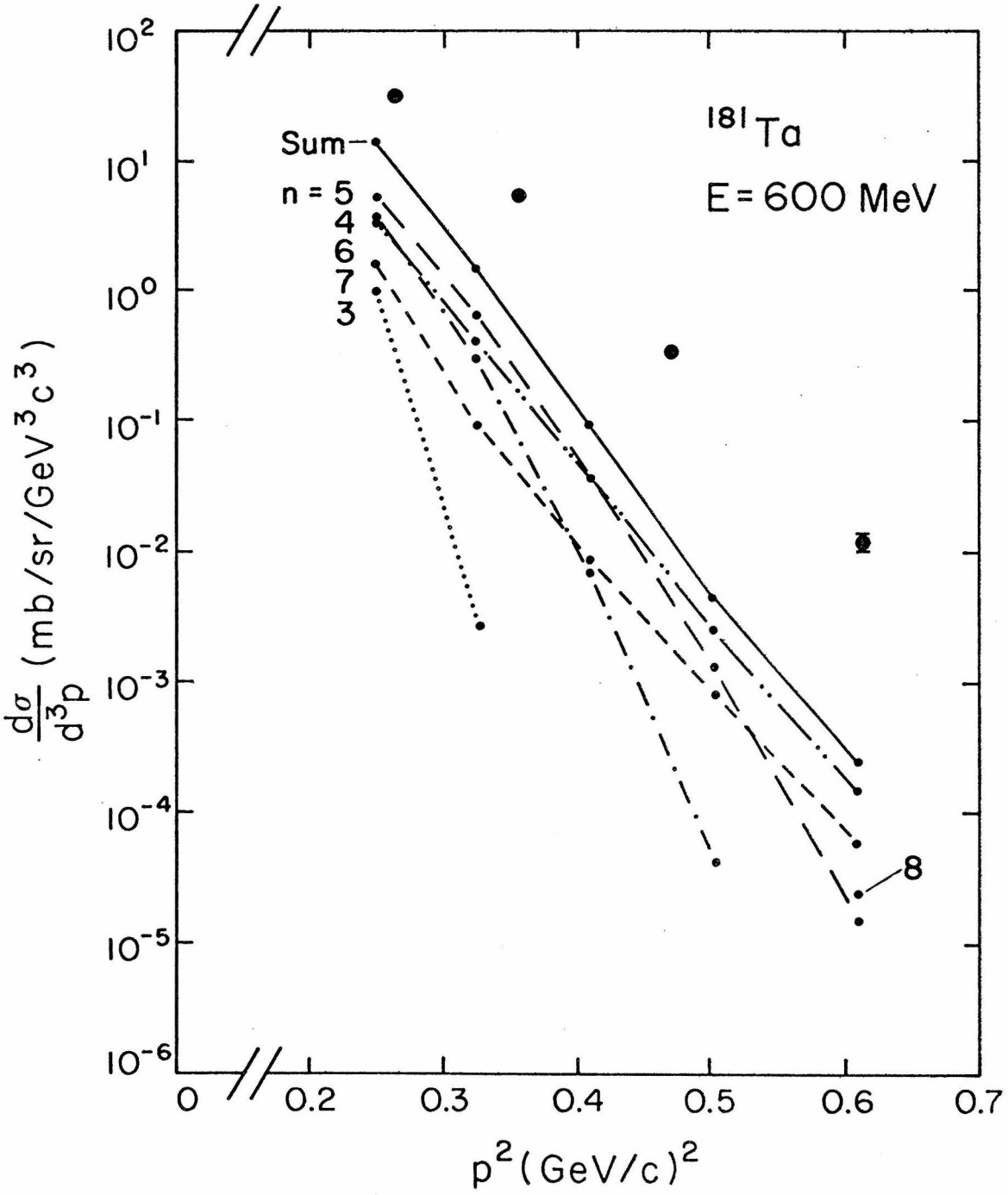
10^2
10^1
10^0
10^{-1}
10^{-2}
10^{-3}
10^{-4}
10^{-5}
10^{-6}
$\frac{d\sigma}{d^3p}$ (mb/sr/GeV^{3}c^3)
Sum
n = 5
4
6
7
3
8
^{181}Ta
E = 600 MeV
0
0.2
0.3
0.4
0.5
0.6
0.7
p^2 (GeV/c)^2